

Exciton interacting with a moiré lattice—polarons, strings, and quantum probing of spin correlations

Aleksi Julku, Shanshan Ding, and Georg M. Bruun

Center for Complex Quantum Systems, Department of Physics and Astronomy, Aarhus University, Ny Munkegade, DK-8000 Aarhus C, Denmark

(Dated: August 6, 2024)

The ability to create and stack different atomically thin transition metal dichalcogenide (TMD) layers on top of each other has opened up a rich playground for exploring new and interesting two-dimensional (2D) quantum phases. As a consequence of this remarkable development, there is presently a need for new sensors to probe these 2D layers, since conventional techniques for bulk materials such as X-ray and neutron scattering are inefficient. Here, we develop a general theory for how an exciton in a TMD monolayer couples to spin and charge correlations in an adjacent moiré lattice created by a TMD bi-layer. Virtual tunneling of charge carriers, assumed for concreteness to be holes, between the moiré lattice and the monolayer combined with the presence of bound hole-exciton states, i.e. trions, give rise to an effective interaction between the moiré holes and the exciton. In addition to the Umklapp scattering, we show that this interaction is spin-dependent and therefore couples the exciton to the spin correlations of the moiré holes, which may be in- as well as out-of-plane. We then use our theory to examine two specific examples where the moiré holes form in-plane ferromagnetic or anti-ferromagnetic order. In both cases, the exciton creates spin waves in the moiré lattice, which we analyse by using a self-consistent Born approximation that includes such processes to infinite order. We show that the competition between magnetic order and exciton motion leads to the formation of a well-defined quasiparticle consisting of the exciton surrounded by a cloud of magnetic frustration in the moiré lattice sites below. For the anti-ferromagnet, we furthermore demonstrate the presence of the elusive geometric string excitations and discuss how they can be observed via their smoking gun energy dependence on the spin-spin coupling, which can be tuned by varying the twist angle of the moiré bi-layer. All these phenomena have clear signatures in the exciton spectrum, and as such our results illustrate that excitons are promising quantum probes providing optical access to the spin correlations of new phases predicted to exist in TMD materials.

I. INTRODUCTION

Transition metal dichalcogenides (TMDs) have emerged as a new and powerful platform for exploring strongly correlated physics in two dimensions (2D). This is due to their rich spin-valley degrees of freedom and useful optical properties [1–6], combined with the possibility to stack two or more monolayers with a lattice mismatch or at a relative angle, which creates a long wavelength moiré potential [7–9]. The low energy physics of such moiré lattices can be described by a highly tunable Fermi-Hubbard model, where many different many-body phases can be realised [10–14]. There has recently been remarkable experimental progress exploring these systems including the observation of a Mott insulating state at unit filling [15, 16] and a possible superconducting state [17], correlated insulating states (generalised Wigner states) at discrete fractional fillings [18–23], as well as the integer and fractional anomalous quantum Hall effects [24, 25]. Since excitons are tightly bound in TMDs, they can for many purposes be regarded as bosons, which together with the electrons realise intriguing new Bose-Fermi mixtures. This has led to the observation of Fermi [26] and Bose polarons [27], and has been predicted to give rise to exciton mediated superconductivity [28–32]. Moiré lattices are naturally triangular and can host a range of magnetic and spin liquid phases [12, 14, 33–35] with spin correlations

predominantly in-plane [35–37]. Measurements of the out-of-plane magnetic susceptibility using an external magnetic field indicate an antiferromagnetic spin-spin coupling in WSe_2/WS_2 [15] and $\text{MoTe}_2/\text{WSe}_2$ [38] bi-layers at unit filling, whereas such measurements reveal ferromagnetic correlations away from the unit filling for a $\text{MoSe}_2/\text{WS}_2$ bi-layer [39]. Transport measurements for a $\text{WSe}_2/\text{WSe}_2$ bi-layer are consistent with a non-magnetic state such as a spin liquid [40].

In order to harness the full potential of these new 2D materials, it is important to have efficient probes for their properties. In particular, having access to the spin correlations of the moiré electrons would be highly useful as they are often one of the defining features of the different magnetic and spin liquid states predicted to be the ground state in moiré systems [12, 14, 34–36, 41–43]. Techniques developed for 3D materials such as X-ray and neutron scattering are inefficient for 2D materials due to the required large sample mass to obtain observable signals [44], and it is difficult to extract the underlying particle correlations from magneto-transport or scanning probes [45].

Inspired by these developments, we explore in this work the properties of an exciton in a TMD monolayer placed on top of a TMD bi-layer forming a moiré lattice. We show that virtual tunneling of holes, which are taken to be the charge carriers, between the moiré lattice and the monolayer gives rise to a strong and spin-dependent

exciton-hole interaction. This is because only holes and excitons with opposite spin interact significantly and can bind to form a trion. We show that this interaction gives rise to Umklapp scattering to first order of the number of exciton-hole scattering events, whereas higher order scattering terms couple the exciton to the spin-spin correlations of the moiré holes. Our theory is then applied to two cases, where moiré holes either form anti-ferromagnetic (AFM) or ferromagnetic (FM) order. The exciton is demonstrated to excite spin waves in both the cases, and to study the exciton spectral function, we employ a strong coupling theory based on a self-consistent Born approximation that includes spin waves to infinite order. We find that these spin wave excitations result in the formation of a well-defined quasi-particle consisting of the exciton dressed by a cloud of magnetic frustration in the moiré lattice sites below. In the case of the AFM, there are also damped excited states, which can be identified as geometric strings due to their characteristic energy dependence on the spin-spin coupling strength in the moiré lattice. Importantly, this dependence can be experimentally probed by changing the twist angle of the moiré bi-layer showing how the flexibility of the TMD setup can be used to detect these elusive states. Since our theory for the interaction between an exciton and the spin and charge degrees of freedom in an adjacent moiré lattice is quite general, our results demonstrate how excitons can be used as non-evasive quantum probes for the new and rapidly growing class of 2D van der Waals materials.

The next sections of our paper are organised as follows. In Sec. II, we describe our setup and the resulting Hamiltonian. Section III analyses the exciton-hole scattering and discusses qualitatively the main physical effects arising from this. Next, we present in Sec. IV a theory, which expands the exciton energy spectrum in terms with an increasing number of exciton-hole scattering events, and we show how the exciton couples to the spin-spin correlations of the moiré holes. In Sec. V, we combine this theory with a non-perturbative Born approximation to describe the cases where the moiré holes form in-plane AFM or FM order. This leads to a physical picture where the exciton creates and absorbs spin waves. Our numerical results including the emergence of polarons, damping, and geometric strings are presented in Sec. VI, and we end in Sec. VII with a discussion and outlook.

II. SETUP

We consider the setup illustrated in Fig. 1(a) where a TMD mono-layer is stacked on top of a TMD bi-layer forming a moiré lattice. We will explore how the spin correlations in the moiré lattice affect an exciton in the mono-layer, which will be referred to as the exciton layer in the following. To avoid the formation of a three-layer moiré system, the probe and moiré layers are separated

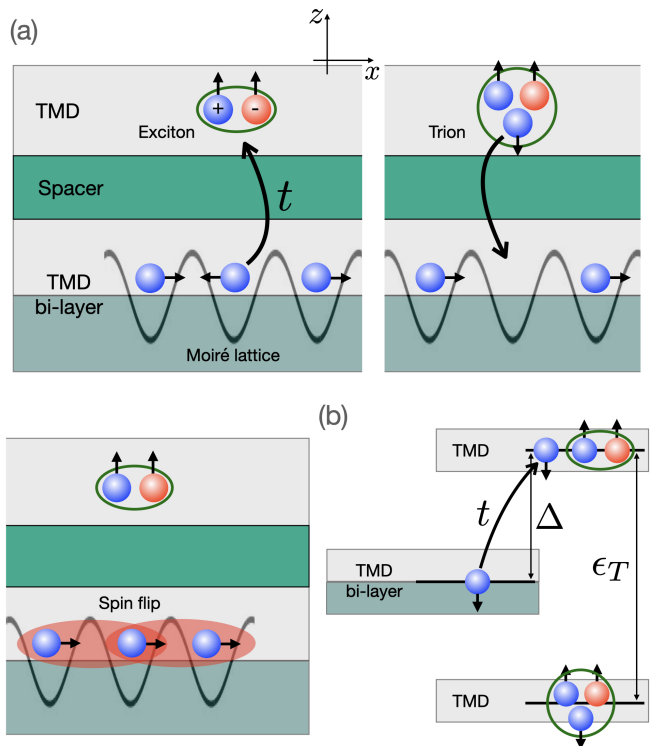


FIG. 1. (a) System considered. A top TMD layer contains an exciton formed by a spin \uparrow hole (blue ball) bound to a spin \uparrow electron (red ball). An adjacent TMD bilayer forms a moiré lattice with one hole per site featuring in-plane spin correlations, which in the figure are taken to form an AFM. A spin \downarrow moiré hole can virtually tunnel to the top layer and form a trion state with the exciton. Since its spin in the trion state is perpendicular to the TMD layers, this can lead to a flip of its in-plane spin when it tunnels back to the moiré lattice. This tunnelling gives rise to an effective exciton-hole interaction that creates magnetic frustration (red ellipses) in the moiré lattice sites below the exciton. (b) Underlying level structure. A spin \downarrow hole in the TMD bi-layer forming the moiré lattice can tunnel to the top TMD layer where its energy is increased by Δ . It can however bind with an exciton thereby lowering its energy by the trion binding energy ϵ_T .

by a spacing layer with energy bands highly detuned by an energy off-set $\tilde{\Delta}$ with respect to the relevant energies.

For concreteness, we assume that the moiré lattice is in the hole doping regime; the analysis for the electron-doping case is completely analogous. Using the Schrieffer-Wolff transformation, we obtain that the tunneling rate of holes between the top layer of the moiré system and the exciton layer is $t \sim \tilde{t}^2/\tilde{\Delta}$, where $\tilde{t} \ll \tilde{\Delta}$ is the interlayer tunneling between the spacer layer and its two neighbouring layers. Further details are given in App. A.

A. Exciton coupled to moiré holes

Without losing generality, we consider a spin-up (\uparrow) exciton in the exciton layer. Note that due to the spin-orbit coupling in the TMDs, the spin quantisation axis is perpendicular to the layers, which we define as the z -axis, see Fig. 1. There are at least two physical effects giving rise to a spin-dependent exciton-hole interaction. First, a \uparrow hole tunneling from the moiré system to the exciton layer can be exchanged with the \uparrow hole bound in the exciton whereas a \downarrow hole cannot. This gives rise to a spin-dependent hole-exciton exchange interaction, which however is quite weak.

We therefore focus on a second effect arising from the fact that the \uparrow exciton interacts predominantly with \downarrow holes. This is because excitons in TMDs are tightly bound and have a small spatial size. The Pauli exclusion principle, which prohibits two holes with the same spin to be at the same position therefore suppresses the probability that a spin \uparrow hole is close to a \uparrow exciton and hence their interaction. The effective Hamiltonian describing the coupling between the moiré system and the exciton layer is

$$H = \sum_{\mathbf{k}} \begin{bmatrix} a_{\mathbf{k}\downarrow}^\dagger & h_{\mathbf{k}\downarrow}^\dagger \\ \epsilon_{\mathbf{k}} + \Delta & t \\ t & \epsilon_{\mathbf{k}} \end{bmatrix} \begin{bmatrix} a_{\mathbf{k}\downarrow} \\ h_{\mathbf{k}\downarrow} \end{bmatrix} + \sum_{\mathbf{k}} \epsilon_{\mathbf{k}}^x x_{\mathbf{k}}^\dagger x_{\mathbf{k}} + \sum_{\mathbf{k}\mathbf{k}'\mathbf{q}} V(\mathbf{q}) x_{\mathbf{k}+\mathbf{q}}^\dagger a_{\mathbf{k}'-\mathbf{q}\downarrow}^\dagger a_{\mathbf{k}'\downarrow} x_{\mathbf{k}}. \quad (1)$$

Here $a_{\mathbf{k}\downarrow}^\dagger$ and $h_{\mathbf{k}\downarrow}^\dagger$ create a \downarrow hole with in-plane momentum \mathbf{k} and kinetic energy $\epsilon_{\mathbf{k}}$ in the exciton layer and top layer of the moiré system respectively, $x_{\mathbf{k}}^\dagger$ creates an exciton in the exciton layer with momentum \mathbf{k} and kinetic energy $\epsilon_{\mathbf{k}}^x = k^2/2m_x$ (m_x being the exciton mass), Δ is the energy off-set between the exciton layer and the moiré system, and $V(\mathbf{q})$ is the interaction between the exciton and the \downarrow holes in the exciton layer. We have ignored the tunneling of \uparrow holes as they are assumed to interact only weakly with the excitons, and we use units where $\hbar = 1$.

B. Moiré bi-layer

In addition to Eq. (1) describing the exciton and its coupling to the moiré holes, we also need a Hamiltonian for the moiré system itself. While our results are quite general, we focus in the rest of the paper on the experimentally relevant case of a half-filled triangular moiré lattice formed by a MoSe₂-WS₂ bilayer. To describe the moiré lattice, we use a microscopic continuum model with interlayer hole tunneling between the MoSe₂ and WS₂ layers [46, 47]. For brevity, we present the details and numerical parameters of these calculations in App. B and simply plot in Fig. 2 the resulting highest valence Bloch bands along high symmetry directions in the moiré Brillouin zone (mBZ) for a twist angle $\theta = 2.5^\circ$ between the two layers. We see that the highest moiré valence band is well separated in energy from the other bands. As we

are interested in the hole-doping regime of the half-filled highest band, we discard the lower bands and describe the moiré holes in the highest valence band with an effective triangular tight-binding model. By accounting also for the repulsive Coulomb interaction between the moiré holes, we can write down an effective many-body moiré Hamiltonian for the moiré holes as

$$H_m = \sum_{ij\sigma} t_{ij}^\sigma h_{i\sigma}^\dagger h_{j\sigma} + \sum_i U_0 h_{i\uparrow}^\dagger h_{i\downarrow}^\dagger h_{i\downarrow} h_{i\uparrow} + \sum_{ij\sigma\sigma'} U_{ij} h_{i\sigma}^\dagger h_{j\sigma'}^\dagger h_{j\sigma'} h_{i\sigma} + \sum_{ij\sigma\sigma'} X_{ij} h_{i\sigma}^\dagger h_{j\sigma'}^\dagger h_{i\sigma'} h_{j\sigma}, \quad (2)$$

where $h_{i\sigma}$ annihilates a hole with spin $\sigma \in \{\uparrow, \downarrow\}$ at moiré lattice site i . The first term in Eq. (2) describes hole hopping, where the matrix elements t_{ij}^σ are obtained by taking the Fourier transform of the energy dispersion of the highest moiré valence band. For small twisting angle θ , corresponding to a large moiré lattice constant, we find as expected that the nearest-neighbor hopping matrix element is by far the largest in magnitude. In Fig. 2 the band dispersion produced by the first term of Eq. (2) with only nearest neighbour hopping (squares) is compared to the original highest valence band. We see that the agreement is quantitative, which justifies the use of the effective single band model given by Eq. (2).

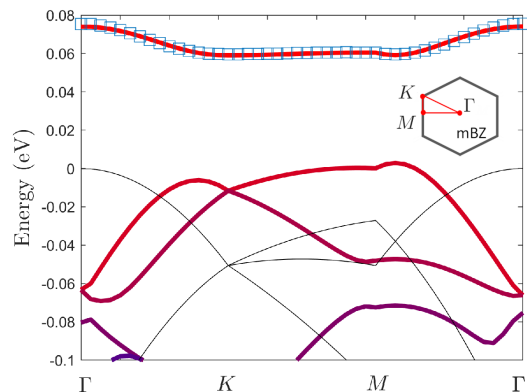


FIG. 2. Energy dispersions (red lines) of the highest spin \downarrow valence Bloch bands of the MoSe₂-WS₂ bilayer along high symmetry directions in the mBZ for twisting angle $\theta = 2.5^\circ$. The black lines are the Bloch bands without the moiré coupling. Squares depict the dispersion of the highest valence band obtained from the nearest-neighbour tight-binding model.

The second, third and fourth terms in Eq. (2) describe, respectively, the on-site, non-local direct and exchange Coulomb interaction between the moiré holes, where the interaction matrix elements U_0 , U_{ij} and X_{ij} are $U_0 = \langle w_i w_i | V_c | w_i w_i \rangle$, $U_{ij} = \langle w_i w_j | V_c | w_i w_j \rangle$, and $X_{ij} = \langle w_i w_j | V_c | w_j w_i \rangle$. Here $V_c(r)$ is the Coulomb interaction and w_i is the Wannier function for the moiré lattice site i [14, 48]. Note that these Wannier states have components in both layers of the moiré bilayer leading to intra- and inter-layer Coulomb matrix elements. A detailed account of these calculations is given in App. B.

As expected, we find that for small twist angles the on-site interaction U_0 is much larger than any other relevant energy scale. For example, for $\theta = 2.5^\circ$ we have $U_0/U_{\text{NN}} \sim 4$ and $U_0/|t_{\text{NN}}^\sigma| \sim 25 \gg 1$ where "NN" refers to the nearest-neighbour terms. It follows that doubly occupied sites are energetically suppressed and that the low energy excitations of the holes at half filling can be described by an extended Heisenberg model

$$H_m = J_1 \sum_{\langle i,j \rangle} \mathbf{s}_i \cdot \mathbf{s}_j + J_2 \sum_{\langle\langle i,j \rangle\rangle} \mathbf{s}_i \cdot \mathbf{s}_j + H_{\text{DM}}. \quad (3)$$

Here, the spin operators read $\mathbf{s}_i = \sum_{\sigma\sigma'} h_{i\sigma}^\dagger \boldsymbol{\sigma}_{\sigma\sigma'} h_{i\sigma'}/2$ where $\boldsymbol{\sigma} = (\sigma_x, \sigma_y, \sigma_z)$ is a vector of the Pauli matrices. Microscopic expressions for the nearest neighbour J_1 and next-nearest neighbour J_2 spin-spin coupling strengths are derived in Ref. [14] and for completeness given in App. B. Using the experimentally realistic parameters for the MoSe₂-WS₂ bilayer resulting in the Bloch bands shown in Fig. 2, we obtain $J_1 \sim 0.23\text{meV}$ ($J_1 \sim 0.95\text{ meV}$) and $J_2 \sim 0.001\text{meV}$ ($J_2 \sim 0.02\text{ meV}$) for the twisting angles $\theta = 2.5^\circ$ ($\theta = 3.3^\circ$).

Our calculations also yield a small imaginary part for the NN hopping matrix elements t_{NN}^σ . This gives a rise to the so-called Dzyaloshinskii-Moriya term $H_{\text{DM}} = J_1 \sum_{\langle i,j \rangle} [(\cos 2\phi - 1)\mathbf{s}_i \cdot \mathbf{s}_j + \sin 2\phi \hat{\ell}_z \cdot (\mathbf{s}_i \times \mathbf{s}_j)]$, where ϕ is the complex phase of t_{NN}^σ [35, 36]. While this term is small for small ϕ and therefore omitted in the subsequent sections, its presence is important since it breaks the $O(3)$ symmetry of the moiré lattice and has been predicted to favour *in-plane* magnetic ordering [35–37].

Note that it is a very challenging to provide a microscopic description of the highly correlated states of electrons in triangular moiré lattices and the microscopic model used may not be quantitatively accurate. This is however not essential for the main results of the present paper; namely that the coupling between an exciton and the in-plane spin correlations of electrons (holes) in a moiré lattice leads to the formation of polarons and geometric strings, which are visible in the exciton spectrum making it a useful quantum probe. Indeed, different values of the spin-spin couplings will of course change our results quantitatively but not qualitatively as long as the underlying phases remain the same.

III. EXCITON-HOLE SCATTERING

While the interaction $V(\mathbf{q})$ in Eq. (1) takes place in the exciton layer between spin \downarrow holes and a spin \uparrow exciton, the tunneling t gives rise to an effective scattering between a spin \downarrow hole in the top moiré layer and an exciton in the exciton layer [49, 50]. Indeed, a spin \downarrow hole in the top moiré layer can tunnel to the exciton layer, interact with the exciton, and subsequently tunnel back to the top moiré layer.

By taking such tunneling processes into account to the lowest order in t/Δ , we show in App. C that the scattering matrix between spin \downarrow holes in the top moiré

layer and a spin \uparrow exciton in the exciton layer is given by $t^2\mathcal{T}/\Delta^2$. Here, \mathcal{T} is the scattering matrix between a hole and an exciton in the exciton layer, which can be evaluated within the ladder approximation as depicted diagrammatically in Fig. 3(a). Since one can to a good approximation ignore the momentum dependence of the interaction $V(\mathbf{q})$ [51], we obtain

$$\mathcal{T}(\mathbf{K}, \omega) = \frac{1}{\Pi(0, \epsilon_T) - \Pi(\mathbf{K}, \omega)}, \quad (4)$$

where $\Pi(\mathbf{K}, \omega)$ is the propagator of an exciton-hole pair in the exciton layer with total momentum and energy (\mathbf{K}, ω) . In Eq. (4), we have replaced the bare interaction strength $V(\mathbf{q})$ with the binding energy $\epsilon_T < 0$ of a trion state consisting of a spin \uparrow electron, a spin \uparrow hole, and a spin \downarrow hole in the exciton layer as explained in more detail in App. C [52–54].

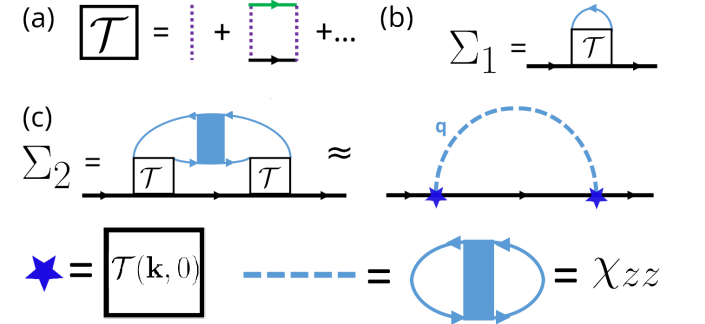


FIG. 3. (a) The scattering matrix for an exciton (black line) and a spin \downarrow hole in the exciton layer (green line) in the ladder approximation, with the dashed purple lines depicting the exciton-hole interaction $V(\mathbf{q})$. (b) The exciton self-energy term Σ_1 . The blue line corresponds to a moiré hole (c) The exciton self-energy term Σ_2 with the blue box indicating correlations between a spin \uparrow and a spin \downarrow hole in the moiré lattice. The star indicates the static scattering matrix and the dashed blue line a spin wave in the moiré system. (d) The self-consistent Born approximation for Σ_2 . The double line is the full exciton Green's function.

Equation (4) takes into account that the interaction $V(\mathbf{q})$ can support a bound state between a \downarrow hole in the exciton layer and a \uparrow exciton, i.e. a trion as illustrated in Fig 1(a). This gives rise to a pole in the scattering matrix at the trion energy, and in order to simplify the subsequent numerical calculations, we expand around this pole writing $\mathcal{T}(\mathbf{k}, \omega) = Z/[\omega - \epsilon_T(\mathbf{k})]$. Here, $\epsilon_T(\mathbf{k}) = \Delta + \epsilon_T + k^2/2m_T$ is the energy of the trion with momentum \mathbf{k} and residue Z with m_T being the trion mass, see Fig. 1(b) and App. C. As discussed further in Sec. VI, the trion energy ϵ_T is in typical experiments well below any relevant energies [55], and we can consequently neglect the frequency dependence of the scattering matrix writing $\mathcal{T}(\mathbf{p}) \equiv \mathcal{T}(\mathbf{p}, \omega = 0)$.

A. Effective interaction

We first discuss heuristically the main physical consequences of the exciton-hole scattering given by Eq. (4). In this way, we can qualitatively describe the main results presented in this paper before getting into the rigorous details of our calculations.

While the scattering matrix given by Eq. (4) is written in the momentum space, it is illuminating to discuss the interaction in the real space. As mentioned above, the moiré holes reside in a triangular moiré lattice described by the operators $h_{i\sigma}$. On the other hand, the parabolic dispersion of the exciton corresponds to a continuum system. However, as we will show explicitly in Sec. IV A, scattering on the moiré holes gives rise a triangular mean-field potential for the exciton with the same periodicity as the moiré lattice. We therefore for the sake of the present discussion introduce the operators γ_i^\dagger creating an exciton at site i in a triangular lattice. Fourier transforming Eq. (4) then yields the effective exciton-hole interaction $V_{\text{eff}} = \sum_{ij} \mathcal{T}(\mathbf{r}_i - \mathbf{r}_j) \gamma_i^\dagger h_{i\downarrow}^\dagger h_{j\downarrow} \gamma_j \simeq \sum_i \mathcal{T}(0) \gamma_i^\dagger \gamma_i h_{i\downarrow}^\dagger h_{i\downarrow}$, where $\mathcal{T}(\mathbf{r})$ is the static exciton-hole scattering matrix in real-space and we have used the fact that the dominant term is the local one with $i = j$. Since we are interested in the case of a half-filled moiré lattice, we have $h_{i\downarrow}^\dagger h_{i\downarrow} = 1/2 - s_{iz}$. Using this gives

$$V_{\text{eff}} \simeq \sum_i \mathcal{T}(0) \gamma_i^\dagger \gamma_i s_{iz} + V_{\text{stat}}, \quad (5)$$

where the last term is a static potential term not important for the present discussion. Since we are focusing on in-plane magnetic order of the moiré holes perpendicular to the z -axis, the s_{iz} operators induce spin rotations as seen explicitly with the identity $s_{iz} = \exp(i\pi s_{iz})/2i$. It follows that Eq. (5) describes an effective interaction where the exciton flips the in-plane spins of the holes below it in the moiré lattice as illustrated in Fig. 4(a). As discussed in Sec. V A and App. F, a rigorous expression for the effective exciton-hole interaction in real space describes the same physics as Eq. (5) and differs mainly by including moiré Bloch wave functions.

As we shall discuss in detail below, this has two main consequences. First, the exciton-hole interaction leads to the creation of a *quasi-particle* consisting of an exciton surrounded by a cloud of magnetic frustration of the moiré holes in its vicinity as illustrated in Fig. 4(a). As we shall see, the energy and mass of this quasiparticle can differ significantly from those of the free exciton, which should be observable using spectroscopy. Second, since the exciton leaves a trace of magnetic frustration in its path as illustrated in Fig. 4(b), it experiences a linear potential with a slope proportional to J_1 . This can trap the exciton resulting in the existence of excitations corresponding to *geometric string states*, in analogy to what has been predicted for a hole moving in an AFM background [56–59]. As we shall discuss in detail below, the moiré bi-layer offers new and promising ways to observe smoking gun features of these elusive states.

In the rest of the paper, we will present a quantitative discussion of these effects.

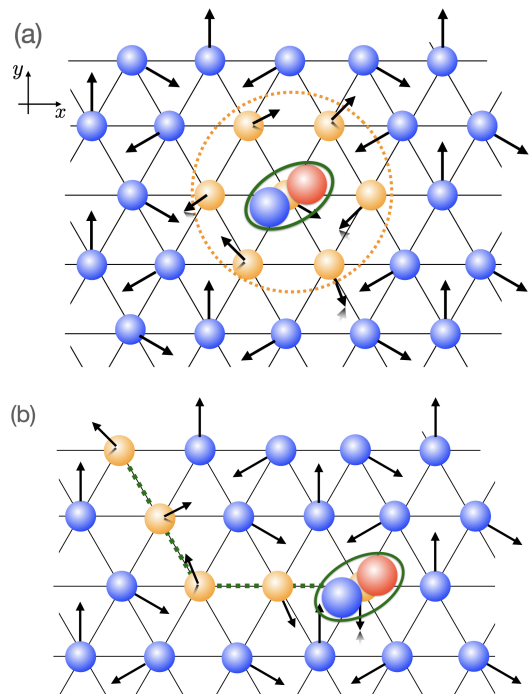


FIG. 4. (a) The exciton-hole interaction Eq. (5) flips spins in a 120° AFM formed by the moiré holes, which leads to the formation of a quasiparticle consisting of an exciton in the top TMD layer and holes with miss-aligned spins (orange balls) in the moiré lattice below. (b) As the exciton moves, it leaves a trace (green dashed line) of mis-aligned spins in the moiré lattice below. This creates a linear potential for the exciton, which supports string-like excitations.

IV. EXCITON SELF-ENERGY

In this section, we set up a strong coupling theory describing how the charge and spin correlations in the moiré lattice affect the exciton. Our diagrammatic approach is based on considering processes with an increasing number of exciton-hole scattering events. That is, we expand the exciton self-energy in increasing orders of the scattering matrix \mathcal{T} , keeping all first and second order diagrams.

A. Umklapp scattering

The exciton self-energy arising from a single exciton-hole scattering event is shown diagrammatically in Fig. 3(b). It describes the creation of uncorrelated holes in the moiré lattice due to the scattering on the exciton

and is given by

$$\begin{aligned} \Sigma_1(\mathbf{p}', \mathbf{p}) &= \frac{t^2}{2\Delta^2} \frac{1}{A} \sum_{\mathbf{q}} \mathcal{T}(\mathbf{p} - \mathbf{q}) u_{\downarrow}^*(\mathbf{q}) u_{\downarrow}(\mathbf{q} + \mathbf{p}' - \mathbf{p}) \\ &\times \left(\frac{1}{2} \delta_{\mathbf{p}' - \mathbf{p}, \mathbf{G}_{\alpha}} - \frac{1}{\sqrt{N}} \langle s_{\mathbf{p}' - \mathbf{p}}^z \rangle \right). \end{aligned} \quad (6)$$

Here, A is the area of the system and $\langle \dots \rangle$ denotes the average with respect to the ground state of the moiré holes. Furthermore, \mathbf{p} (\mathbf{p}') is the incoming (out-going) exciton momentum, which is conserved up to the reciprocal moiré lattice vectors \mathbf{G}_{α} since the exciton scatters on the \downarrow holes residing in the lattice. In deriving Eq. (6), we have expanded the operator $h_{\mathbf{k}\downarrow + \mathbf{G}_{\alpha}}^{\dagger}$, which creates a hole with momentum $\mathbf{k} + \mathbf{G}_{\alpha}$ in the top layer of the moiré system, as

$$\begin{aligned} h_{\mathbf{k} + \mathbf{G}_{\alpha}\downarrow}^{\dagger} &= \sum_n u_{n\downarrow}(-\mathbf{k} - \mathbf{G}_{\alpha}) h_{n\mathbf{k}\downarrow} \simeq u_{1\downarrow}(-\mathbf{k} - \mathbf{G}_{\alpha}) h_{1\mathbf{k}\downarrow}^{\dagger} \\ &= u_{\downarrow}(-\mathbf{k} - \mathbf{G}_{\alpha}) \frac{1}{\sqrt{N}} \sum_j e^{i\mathbf{k}\cdot\mathbf{r}_j} h_{j\downarrow}^{\dagger}. \end{aligned} \quad (7)$$

Here \mathbf{k} is a momentum in the mBZ, $h_{n\mathbf{k}\downarrow}^{\dagger}$ creates a hole in moiré Bloch band n with momentum \mathbf{k} and spin \downarrow , and $u_{n\downarrow}(\mathbf{k})$ is the projection of the corresponding Bloch function to the top moiré layer. The approximation in the first line of Eq. (7) corresponds to projecting to the highest moiré valence band ($n = 1$), since it is well separated from the other moiré bands as discussed in Sec. II B and shown in Fig. 2. In the second line we have Fourier transformed to the real space with N being the number of moiré sites, and suppressed the band index of the Bloch functions. Finally, we have in Eq. (6) used the identity $h_{i\downarrow}^{\dagger} h_{i\downarrow} = 1/2 - s_{iz}$ valid at half-filling, and defined $s_{\mathbf{p}}^z = \sum_j \exp(-i\mathbf{p}\cdot\mathbf{r}_j) s_j^z / \sqrt{N}$. In App. D 1, we give further details regarding the derivation of Eq. (6).

The first term in Eq. (6) describes Umklapp scattering of the exciton on holes residing in the moiré lattice in the Mott phase and it is present even when there is no magnetic order. The effects of the Umklapp scattering on the exciton spectrum have recently been used to probe the formation of an electronic Wigner crystals and stripe phases at various filling fractions in moiré lattices [16, 19, 21, 23, 60, 61]. The second term of Eq. (6), proportional to $\langle s_{\mathbf{p}}^z \rangle$, couples the exciton to any out-of-plane magnetic order of the moiré holes. It was recently shown that this term gives rise to observable effects on the exciton spectrum that can be used to probe such out-of-plane magnetic order [62].

In the present work, we instead wish to explore how the exciton couples to spin correlations in the moiré lattice, which can be in an *arbitrary* direction. This is motivated by the fact that the Dzyaloshinskii-Moriya spin coupling has been predicted to favor in-plane magnetic ordering [35–37], for which the Umklapp scattering term given by Σ_1 is insensitive.

B. Coupling to spin correlations

We therefore need to analyse how the exciton couples to the spin correlations in the moiré lattice, which first occurs to second order in the exciton-hole scattering. Such processes are described by the self-energy term Σ_2 shown in Fig. 3(c), where the exciton creates an electron-hole pair in the moiré lattice, which is strongly correlated due to interactions in the moiré lattice proportional to U . As detailed in App. D 2, a long calculation gives

$$\begin{aligned} \Sigma_2(\mathbf{p}', \mathbf{p}, i\omega_n) &= \frac{t^4}{\Delta^4} \frac{T}{A} \sum_{i\omega_m} \sum_{\mathbf{q}} \mathcal{G}(\mathbf{p} - \mathbf{q}, i\omega_n - i\omega_m) \\ &\times g(\mathbf{p}, -\mathbf{q}) g(\mathbf{p} - \mathbf{q}, \mathbf{p}' - \mathbf{p} + \mathbf{q}) \chi_{zz}(\mathbf{q}, i\omega_m) \delta_{\mathbf{p}', \mathbf{p} + \mathbf{G}_{\alpha}}. \end{aligned} \quad (8)$$

Here $\mathcal{G}(\mathbf{q}, i\omega_m)$ is the exciton Green's function, $\omega_n = 2\pi nT$ ($n = 0, \pm 1, \dots$) are bosonic Matsubara frequencies and T is the temperature. We have defined the vertex function $g(\mathbf{p}, -\mathbf{q}) = \sum_{\mathbf{k}} \mathcal{T}(\mathbf{p} - \mathbf{k}) u^*(\mathbf{k}) u(\mathbf{k} + \mathbf{q})$ for an exciton with momentum \mathbf{p} exciting a particle-hole pair with total momentum \mathbf{q} in the moiré lattice.

Importantly, $\chi_{zz}(\mathbf{q}, i\omega_m)$ is the Fourier transform of the correlation function $\chi_{zz}(\mathbf{r}_i - \mathbf{r}_j, \tau) = \langle T_{\tau} s_i^z(\tau) s_j^z(0) \rangle$ where τ (T_{τ}) is the imaginary time (time ordering operator). Equation (8) therefore explicitly demonstrates that the exciton is coupled to spin-spin correlations of the moiré holes via the second order exciton-hole scattering processes. Since these spin correlations can be in an arbitrary direction, i.e. in- as well as out-of-plane, this opens up a way to optically detect states with in-plane magnetic order and states with more subtle spin correlations by measuring the exciton spectrum. Equation (8) is therefore a main result of our paper.

V. IN-PLANE FERROMAGNETIC AND ANTIFERROMAGNETIC ORDER

Having developed a theory describing how the exciton couples to spin correlations of the holes in the moiré lattice, we now demonstrate that this can strongly affect its properties. We consider two concrete examples: one where the moiré holes form in-plane AFM order and one where they form FM order.

A. Anti-ferromagnet

The values of J_1 and J_2 given in Sec. II B favor a 120° antiferromagnetic AFM ground state over other possible states such as spin liquids [35, 41, 42, 63]. By using linear spin wave theory (LSWT) to describe this 120° AFM phase, we can write Eq. (3) as

$$H_m = \sum_{\mathbf{k}} \omega_{\mathbf{k}} b_{\mathbf{k}}^{\dagger} b_{\mathbf{k}}, \quad (9)$$

where $b_{\mathbf{k}}^{\dagger}$ creates a bosonic spin wave in the AFM with crystal momentum \mathbf{k} and energy $\omega_{\mathbf{k}} =$

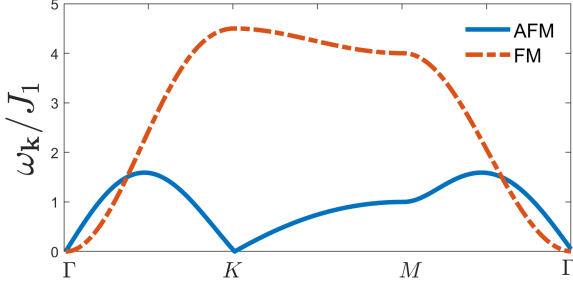


FIG. 5. Spin wave spectrum of the moiré holes obtained from LSWT for the AFM (blue solid line) and FM (red dashed line) states as a function of momenta along high symmetry directions in the mBZ.

$3J_1\sqrt{(1-\gamma_{\mathbf{k}})(1+2\gamma_{\mathbf{k}})}/2$. Here $\gamma_{\mathbf{k}} = \sum_{\delta} \cos(\mathbf{k} \cdot \delta)/6$ is the structure factor with the sum taken over the six nearest-neighbor links δ in the triangular moiré lattice [64], and the small next-nearest coupling J_2 is neglected. We have in Fig. 5 plotted $\omega_{\mathbf{k}}$ as a blue solid line along the high-symmetry points of the mBZ. For small k the spectrum is isotropic and linear with $\omega_{\mathbf{k}} = ck$ where $c = 3^{3/2}J_1a_m/4$ is the speed of the spin waves, and a_m is the moiré lattice constant. We note that linear spin wave theory accurately captures the low energy excitations of a triangular AFM in spite of its inherent geometric frustration [65, 66].

Since the magnetic order is taken to be in-plane, i.e. perpendicular to the z -axis, we have $s_{\mathbf{k}}^z = i(u_{\mathbf{k}} - v_{\mathbf{k}})(b_{-\mathbf{k}}^\dagger - b_{\mathbf{k}})/2$ within LSWT, where $u_{\mathbf{k}} = \sqrt{\frac{2+\gamma_{\mathbf{k}}}{2\sqrt{(1-\gamma_{\mathbf{k}})(1+2\gamma_{\mathbf{k}})}}} + \frac{1}{2}$ and $v_{\mathbf{k}} = \text{sign}(\gamma_{\mathbf{k}})\sqrt{\frac{2+\gamma_{\mathbf{k}}}{2\sqrt{(1-\gamma_{\mathbf{k}})(1+2\gamma_{\mathbf{k}})}}} - \frac{1}{2}$ are coherence factors. It follows that $\chi_{zz}(\mathbf{k}, \tau)$ is proportional to $\langle T_{\tau}[b_{-\mathbf{k}}^\dagger(\tau) - b_{\mathbf{k}}(\tau)][b_{-\mathbf{k}}^\dagger(0) - b_{\mathbf{k}}(0)] \rangle$. Equation (8) therefore describes how the motion of the exciton creates and annihilates spin waves in the adjacent moiré AFM, since it couples differently to spin \uparrow and \downarrow holes. This result is the quantitative momentum space version of the heuristic real space arguments given in Sec. III A. A precise real space version of Eq. (8) is given in App. F by Fourier transforming the exciton-hole interaction to real space. It differs from the heuristic expression Eq. (5) mainly by including moiré Bloch wave functions but describes the same physics.

The spin susceptibility is within the LSWT straightforwardly calculated to be

$$\chi_{zz}(q) = -\frac{1}{4} \left[\frac{(u_{\mathbf{q}} - v_{\mathbf{q}})^2}{iq_n - \omega_{\mathbf{q}}} - \frac{(u_{\mathbf{q}} + v_{\mathbf{q}})^2}{iq_n + \omega_{\mathbf{q}}} \right] \quad (10)$$

where iq_n is a bosonic Matsubara frequency. Technically, we have in this section used LSWT to express the strong particle-hole correlations in the moiré lattice in terms of low-energy spin waves, which is illustrated diagrammatically in Fig. 3(c).

B. Ferromagnet

As has been shown [14], moiré bi-layers can, depending on the system parameters such as the twist angle, specific TMD materials, and the dielectric constant of the surrounding medium, also feature negative values for J_1 , which imply that the holes form a ferromagnet at half filling. We therefore also examine the case of an in-plane FM order assuming a negative value of J_1 in (3). In this case, the LSWT Hamiltonian is still given by Eq. (9) but with the spectrum $\omega_{\mathbf{k}} = 3J_1(\gamma_{\mathbf{k}} - 1)$, see red dashed line in Fig. 5. This excitation spectrum is gapless at $\mathbf{k} = 0$ and quadratic at small momenta, i.e. $\omega_{\mathbf{k}} = J_1a_m^2k^2$ for $\mathbf{k} \rightarrow 0$. The coupling of these spin waves to the exciton via the self-energy Σ_2 can now be calculated in exactly the same way as for the AFM described in Sec. V A, but now with the coherence factors $u_{\mathbf{k}} = 1$ and $v_{\mathbf{k}} = 0$. We shall demonstrate below that it follows from the low energy linear and quadratic spin wave spectra of the AFM and FM that their effects on the exciton spectrum exhibit qualitative differences.

C. Self-consistent Born approximation

As we saw above, the motion of the exciton leads to the emission and annihilation of spin waves in the in-plane magnetic state of the moiré holes. This is closely analogous to the motion of a hole in an AFM background at half filling, which has been studied intensely for decades and is relevant to high temperature and unconventional superconductors [67, 68]. An important result of this large body of research is that a single hole moving in an AFM background is accurately described within the t - J model by the so-called self-consistent Born approximation (SCBA) [69–73]. Remarkably, this holds even for strong interactions, triangular lattices [64], and non-equilibrium dynamics [74].

Due to the close connections with the motion of a hole in an AFM, we expect that an exciton interacting with an in-plane magnetically ordered state is also accurately described by the SCBA. We therefore adopt this approach to the problem at hand, which amounts to using the self-consistent exciton Green's function

$$\mathcal{G}(\mathbf{p}', \mathbf{p}, i\omega_n) = \frac{1}{i\omega_n - \epsilon_{\mathbf{p}}^x - \Sigma(\mathbf{p}', \mathbf{p}, i\omega_n)} \quad (11)$$

when evaluating Eq. (8) with $\Sigma(\mathbf{p}', \mathbf{p}, i\omega_n) = \Sigma_1(\mathbf{p}', \mathbf{p}) + \Sigma_2(\mathbf{p}', \mathbf{p}, i\omega_n)$. This approach is illustrated diagrammatically in Fig. 6. The resulting self-energy term Σ_2 given by Eq. (8) has the same mathematical structure as in case of a single hole moving in an AFM background described by the SCBA [69–73]. Note that the SCBA goes beyond the second order by summing a subset of terms to infinite order in the exciton-hole scattering events, characterised by the so-called rainbow diagrams shown in Fig. 6. In this way, SCBA is able to quantitatively account for strong interaction effects regarding hole motion in AFMs, and

we expect the same to be the case for the motion of an exciton strongly interacting with in-plane magnetically ordered moiré system.

$$\Sigma_2 = \text{[Diagram showing a double line equal to a sum of diagrams: a dashed arc, a dashed arc with a solid line, and a dashed arc with two solid lines, followed by an ellipsis.]}$$

FIG. 6. The self-consistent Born approximation for Σ_2 . The double line is the full exciton Green's function.

VI. NUMERICAL RESULTS

Having set up a strong coupling formalism for an exciton interacting with the moiré holes forming in-plane magnetic order, we are now ready to present results obtained by numerically solving Eqs. (6), (8), and (11) self-consistently. The spin-spin correlation function in Eq. (8) is calculated from Eq. (10) using the spin wave spectrum and coherence factors for either the AFM or the FM. Motivated by recent experiments [55], we take $\epsilon_T = -25$ meV and $\Delta = 8$ meV so that the pole of the \mathcal{T} -matrix is at $\epsilon_p(\mathbf{k}) \sim -17$ meV for small momenta. Since the spin wave energies are of the order $J_1 \sim 0.1$ meV and, as shown below, the relevant exciton energies are in the range of a few meV, we can safely neglect the frequency dependence of the exciton-hole scattering matrix, which justifies the approximation introduced in Sec. III. Finally, we use $t \sim 3$ meV for the hole tunneling parameter between the moiré and exciton layers, which is an experimentally realistic value as discussed in App. A, and consider zero-temperature. Details of the numerical evaluation of the exciton self-energy using the SCBA are provided App. E.

A. Anti-ferromagnet

We first discuss the case of a moiré AFM by using the corresponding spin wave spectrum and coherence factors with a value of J_1 obtained as in Sec. II B. Figure 7(a) shows the diagonal exciton spectral function $A(\mathbf{p}, \omega) = -2 \text{Im}[\mathcal{G}(\mathbf{p}, \mathbf{p}, \omega + i0^+)]$ obtained from the SCBA as a function of energy ω and momentum \mathbf{p} for the twist angle $\theta = 3.0^\circ$. For comparison, we also plot in Fig. 7(a) the non-interacting exciton dispersion $\epsilon_{\mathbf{k}}^x = k^2/2m_x$ as a solid red line and the dispersion obtained including only the Umklapp term Σ_1 in the exciton self-energy as a red dotted line. This shows that the Umklapp scattering increases the exciton energy for small momenta with respect to its non-interacting energy. It can be understood from the fact that the exciton-hole scattering matrix effectively corresponds to a repulsive interaction, since the trion energy $\epsilon_T = -25$ meV is well below any relevant energy. As detailed in App. D 1, one can show that the

zero-momentum energy shift due to the Umklapp potential is of the order $\mathcal{O}(t^2 Z/\Delta^2 |\epsilon_T| a_m^2)$.

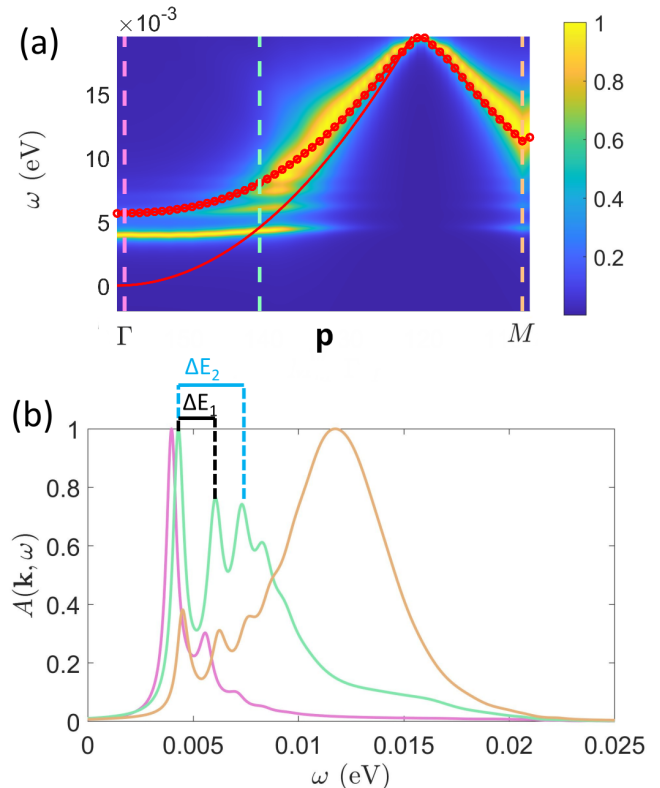


FIG. 7. Exciton spectral function $A(\mathbf{p}, \omega)$ for the twist angle $\theta = 3^\circ$ and an in-plane AFM. Panel (a) presents $A(\mathbf{p}, \omega)$ as a function of the frequency and momentum along the straight path connecting the Γ and M points in the mBZ. The red solid/dotted line gives the exciton dispersion in the absence/presence of the Umklapp scattering term Σ_1 but without the Σ_2 term. Panel (b) shows the spectral function as a function of frequency for fixed momenta given by the vertical lines in (a).

Consider next the spectral function when the full self-energy $\Sigma_1 + \Sigma_2$ is used, which takes into account the scattering on the spin waves to infinite order through the self-energy term Σ_2 . First, we see from Fig. 7 that the spectral function exhibits a sharp peak for small momenta. This peak corresponds to a quasi-particle consisting of the exciton dressed by spin waves in the moiré AFM as illustrated in Fig. 4(a), and it quantitatively confirms the prediction regarding its existence in Sec. III A. We denote this quasiparticle as an exciton-polaron in analogy with what has been done for an exciton coupled to electrons or other distinguishable excitons [26, 27]. In contrast to the Umklapp term Σ_1 , Σ_2 decreases the energy $\epsilon_{\mathbf{p}}^P$ of the exciton-polaron. This follows from the fact that Σ_2 describes the coupling to higher energy states containing spin waves as described through the SCBA. We moreover see that the dressing by the spin waves significantly increases the effective mass m^* of the quasi-particle making

its dispersion flat.

For larger momenta, Fig. 7(a) shows that the quasiparticle peak becomes significantly broadened corresponding to a short lived quasiparticle. Physically, this decay sets in when the energy of the exciton-polaron $\epsilon_{\mathbf{p}}^P$ is sufficient to scatter resonantly on the spin wave spectrum, i.e. when $\epsilon_{\mathbf{p}}^P \geq \min_{\mathbf{q}}[\omega_{\mathbf{q}} + \epsilon_{\mathbf{p}-\mathbf{q}}^P]$. Figure 7(a) furthermore shows that when the damping sets in, the maximum of the broad continuum approaches the Umklapp-dispersion of the exciton. The presence of the sharp quasi-particle peak for small momenta and a broadened spectrum for larger momenta is further illustrated in Fig. 7(b), which plots the spectral function as a function of ω for a number of selected momenta indicated by the vertical dashed lines in Fig. 7(a).

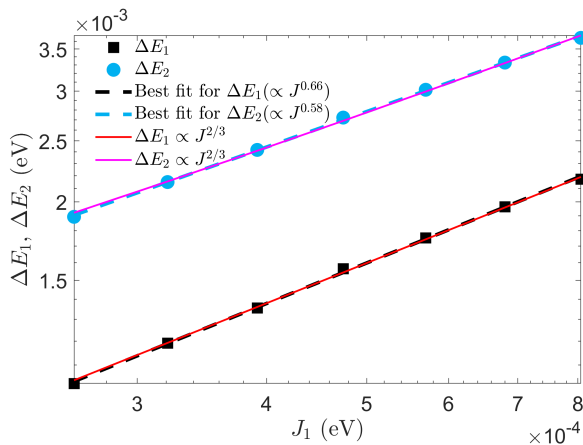


FIG. 8. Log-log plot of the two lowest excitation energies ΔE_1 and ΔE_2 (see Fig. 7) as a function of J_1 for the momentum $\mathbf{p} = 0.35\mathbf{k}_M$. Black squares/blue circles are numerical results, and the dashed lines show the power law fits $\Delta E_i = \beta_i J_1^{\alpha_i}$ where α_i and β_i are the fitting parameters. For ΔE_1 and ΔE_2 , we obtain $\alpha_1 = 0.66$ and $\alpha_2 = 0.58$. The solid lines show the geometric string prediction $\Delta E_i \propto J_1^{2/3}$ with γ_i a fit parameter. The variation in the nearest neighbour spin coupling J_1 corresponds to sweeping the twist angle from 2.6° to 3.2° .

In addition to the sharp quasi-particle peak, Fig. 7 shows a number of intriguing broader peaks appearing at higher energy for small momenta. They correspond to excited states with an energy and decay rate given by the peak center and width respectively. To analyse their physical origin, we plot in Fig. 8 the two lowest excitation energies ΔE_1 and ΔE_2 (see Fig. 7) as a function of J_1 for the momentum $\mathbf{p} = 0.35\mathbf{k}_M$. In addition to the numerical data, we present as the dashed lines the best power-law fits $\Delta E_i \propto J_1^{\alpha_i}$, where $\alpha_1 = 0.66$ and $\alpha_2 = 0.58$ for ΔE_1 and ΔE_2 , respectively. These fits are close to a $J_1^{2/3}$ scaling expected for the so-called geometric string excitations [56–59], which is therefore also plotted in Fig. 8, showing a very good agreement with the numerical results.

By following the the same logic as for the case of a hole

hopping in an AFM background [56–59], such a scaling of ΔE_1 and ΔE_2 can be taken as a fingerprint of geometric string excitations. As we discussed in Secs. III A and V A and illustrated in Fig. 4(b), the exciton leaves a trail of spin flips in the moiré lattice sites as it moves around. Since these spin flips cause an energy penalty of the order of J_1 , the exciton experiences an effective linear potential giving rise to Airy-like eigenstates with the corresponding eigen-energies proportional to $J_1^{2/3}$. A very attractive feature of the present setup is that one can tune J_1 by changing the twisting angle of the moiré bi-layer. This allows one to experimentally verify the smoking gun $J_1^{2/3}$ energy scaling of string excitations, which has turned out to be very difficult to realize for holes in AFMs. In fact, the range of J_1 values shown in Fig. 8 corresponds to scanning the twist angle from $\theta = 2.6^\circ$ to $\theta = 3.2^\circ$ in the MoSe₂-WS₂ bilayer. Hence, our results show how the flexibility of TMDs may allow for a detection of the elusive string excitations. Finally, we emphasize that it is essential to use the non-perturbative SCBA to describe the string excitations. Indeed, as is shown explicitly App. G they are completely missed by second order perturbation theory.

In Fig. 14 in App. E, we plot the exciton spectral function along other high symmetry directions in the mBZ. It exhibits the same features, i.e. a clear exciton-polaron quasiparticle peak and broader peaks coming from excited geometric string states, which demonstrates that these states appear throughout the mBZ.

B. Ferromagnet

We now turn to the case where the moiré holes form an in-plane FM, which we describe by flipping the sign of J_1 . In Fig. 9 we show the resulting exciton spectral function for $J_1 = -0.54$ meV. As for the case of an AFM, we see a clear exciton-polaron quasiparticle with energy above the bare exciton but below that predicted by the Umklapp scattering, and with a large effective mass. This quasiparticle furthermore becomes strongly damped for larger momenta due to scattering on the spin waves, where its dispersion approaches the exciton energy given by the Umklapp scattering.

Compared to the case of an AFM, the most striking difference is the absence of string excitations in the exciton spectrum. This is somewhat surprising since the basic ingredients leading to the presence of such excitations seem to be present for the FM too, i.e. the exciton leaves a string of magnetic frustration in its wake leading to a linear potential. We conjecture that this string picture is nevertheless invalid for the FM, since an initially localised magnetic frustration rapidly spreads out in real space due to the quadratic low energy dispersion of the spin waves. This aspect is discussed further in App. F.

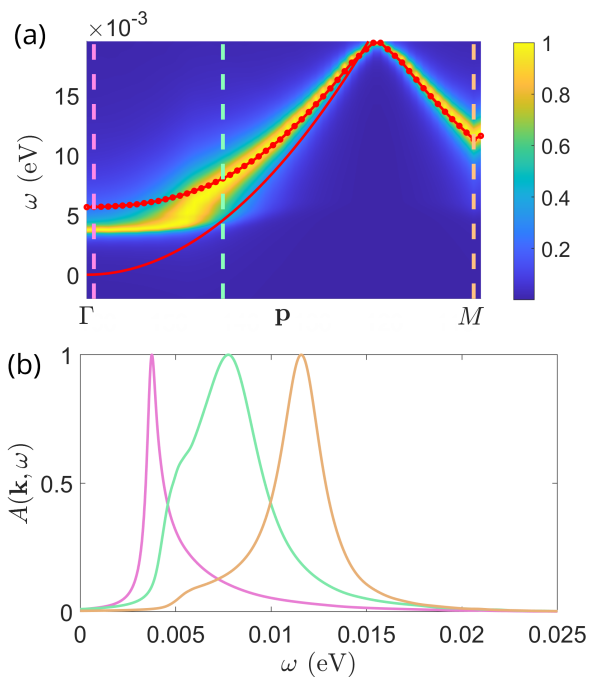


FIG. 9. Exciton spectral function $A(\mathbf{p}, \omega)$ for $\theta = 3^\circ$ for an in-plane FM. Panel (a) presents $A(\mathbf{p}, \omega)$ as a function of the frequency and momentum along the path connecting the Γ and M points in the mBZ. The red solid/dotted line gives the exciton dispersion in the absence/presence of the Umklapp scattering term Σ_1 but without the Σ_2 term. Panel (b) shows the spectral function as a function of frequency for fixed momenta given by the vertical lines in (a).

VII. DISCUSSION AND OUTLOOK

In this work, we developed a general theory for the coupling between an exciton in a TMD monolayer and the spin and charge degrees of freedom in an adjacent moiré lattice formed by a TMD bilayer. Using this theory combined with a non-perturbative self-consistent Born approximation, we explored the coupling between the exciton and spin waves in a half-filled moiré lattice hosting an in-plane AFM or FM order. We showed that this gives rise to the formation of quasiparticle states (polarons) consisting of the exciton surrounded by magnetic frustration in the moiré lattice, damping, as well as geometric string states.

The predicted emergence of a well-defined polaron adds to the list of interesting quasiparticles that can be realised with excitons in TMDs, which includes the experimentally observed Fermi and Bose polarons [26, 27]. The polarons in the present paper are closely related to the magnetic polarons consisting of a mobile hole in a AFM lattice, which play a fundamental role for charge transport in 2D quantum materials including high temperature and unconventional superconductors [67, 68]. We note that as opposed to these materials, the flexibility of TMD bi-layers allows one to tune the nearest neighbor

spin-spin coupling constant by changing the twist angle. This opens up the possibility to observe the elusive string excitations via their the smoking gun energy scaling.

Since we predict clear and observable changes of the exciton spectrum, our results have intriguing perspectives for using excitons as much needed quantum sensors for the *spin* correlations of the rapidly growing class of 2D van der Waals materials. It has previously been shown how the first order mean-field term Σ_1 gives rise to Umklapp scattering branches in the exciton spectrum signalling Wigner crystallisation [23] as well as out-of-plane magnetic order [62]. Here, we demonstrate that higher order terms included in Σ_2 couple the exciton to spin correlations, which can be in any direction and do not have to exhibit long range order. Also, it was recently shown that the in-plane AFM order increases the effective mass of an exciton residing in the moiré lattice [75], and that the spatial periodicity related to different charge and magnetically ordered states influences the plasmon spectrum of moiré systems through the band folding [45]. Finally, the possible magnetic ground states of a RuCl₃ monolayer were shown to change due to the hybridisation with an adjacent graphene layer and giving rise to graphene magneto-resistance [76]. Major strengths of our probe setup include that it gives access to spin correlations, which is essential for identifying interesting phases with no long-range order, and that the exciton probe is non-evasive.

Experimentally, the excitons close to the Γ point can be probed by optical means where a resolution of the order of a few meVs has been achieved in TMDs [23, 62]. This is sufficient to clearly observe the spectral features we predict without significant broadening, which could otherwise be significant due to a finite exciton lifetime for nearly degenerate conduction bands [77]. The spectral features away from the Γ point are accessible using electron energy-loss spectroscopy (EELS), which has recently been used to measure the exciton spectrum in a monolayer WSe₂ [78]. While the energy resolution achieved in this experiment for non-zero momenta is not sufficient to detect the spectral features we predict such as the string states, the experimental techniques are improving rapidly and much higher precision is indeed expected in the future [78]. We also note that since the effects on the exciton spectrum increase with the exciton-electron(hole) interaction strength, they can be much larger and therefore more easily resolved experimentally than shown in Figs. 7 and 9. Finally, the spectral signal from the probe and moiré layers can easily be distinguished as they are well separated in energy [19].

One interesting phase with no long range order but subtle and non-trivial correlations is the Dirac spin liquid, which is a strong candidate for the ground state of the triangular $J_1 - J_2$ Heisenberg model in certain parameter regimes [41, 42]. It would be interesting to explore how the exciton couples to the low energy degrees of freedom of this phase such as spinon excitations, and in what ways this shows up in the exciton spectrum. Spin liquids

should be within experimental reach in TMD bi-layers since they naturally realise a triangular lattice, and since the ratio J_2/J_1 is tunable via the twist angle and the screening of the Coulomb interactions [14]. There likely are many other interesting effects to observe such as for instance a cascade of phase transitions as seen in magic angle graphene [79].

The results presented here open up several other promising research directions. One can use the Feshbach resonance mediated by the trion state to increase the interaction between the exciton and the moiré holes and thereby the effects on the exciton spectrum. This is achieved by tuning the trion energy via the energy offset Δ [49, 50]. Since the static approximation for the exciton-hole scattering matrix used in the present paper is insufficient to analyse this, one must instead keep the full frequency dependence, which is a technically challenging problem. Our results also raise the fundamental questions regarding what properties of the magnetic environment are necessary to stabilise geometric string excitations. Another interesting research topic is how to use excitons pinned in a moiré lattice, as has been achieved experimentally [80–82], to create probes with spatial resolution. Pinning several excitons could furthermore enable powerful and highly useful multiplex sensors capable of simultaneously measuring electron/hole correlations at two or more spatial positions. The hybridisation of the excitons with photons in an optical cavity to form polaritons [83] would have several interesting several effects such as the quantum state of the moiré system being imprinted on the outgoing light. Finally, we considered in the present paper a single exciton, which does not change the quantum state of the moiré lattice in the thermodynamic limit. Experimentally, this corresponds to the limit where the density of excitons is much smaller than the electron density in the moiré lattice. This basic idea has also been used by many experimental groups exploring a few mobile impurity atoms forming so-called polarons by scattering on atoms in their neighborhood in a large surrounding quantum degenerate atomic gas [84]. It would be interesting in the future to consider different exciton and electron concentrations, which will realise new and intriguing Bose-Fermi mixtures.

ACKNOWLEDGMENTS

This work was supported by the Danish National Research Foundation through the Center of Excellence “CCQ” (Grant no. DNR156).

Appendix A: Hole tunneling between the moiré system and the exciton layer

To decrease the hole tunneling between the moiré system and the TMD monolayer and prevent the formation of a large three-layer moiré lattice, we propose to

apply a 30° -rotated WS_2 monolayer as a barrier between the moiré system and the exciton layer. Due to a large rotation angle of the barrier WS_2 layer, its energy band structure is highly detuned by an energy offset $\tilde{\Delta}$ with respect to the relevant energies of the moiré system and the monolayer MoSe_2 . As a result, one can use the Schrieffer-Wolff transformation to estimate the hole tunneling strength between the moiré system and the ML MoSe_2 as $t \sim \tilde{t}^2/\tilde{\Delta}$, where \tilde{t} is the interlayer tunneling parameter between the spacer layer (WS_2) and its two neighbouring MoSe_2 layers [see Fig. 4(b)]. The energy off-set of the valence band edges between un-rotated MoSe_2 and WS_2 layers is around $V \sim 270$ meV [46]. Moreover, the rotation by 30° shifts the energies of the electron states of WS_2 that momentum-match with the relevant states of the neighbouring MoSe_2 layers, by around ~ 1 eV [85]. Hence, we get a rough estimate $\tilde{\Delta} \sim 0.7\text{-}0.8$ eV. On the other hand, if we use $\tilde{t} \sim 50$ meV given in Ref. [46], we have $t = \frac{\tilde{t}^2}{\tilde{\Delta}} \sim 3$ meV. This value can be tuned significantly by for example choosing some other material for the spacer layer or by changing the rotation angle of the spacer.

Appendix B: Moiré Hamiltonian

In this section, the moiré Hamiltonian for electrons is derived in case of a hetero-bilayer by using the continuum model deployed in Refs. [46, 47]. In this model, the long-wavelength moiré potential arises due to interlayer tunneling processes.

We consider a TMD heterobilayer and label the two layers as L1 and L2. For concreteness, we take L1 to be a MoSe_2 and L2 a WS_2 monolayer. The MoSe_2 and WS_2 monolayers have a hexagonal Brillouin zone (BZ) and feature direct band gaps at the K and K' -valleys. For two layers, the K -valleys are at $\mathbf{k} = [4\pi/(3a_1), 0] \equiv \mathbf{K}_1$ and $\mathbf{k} = [4\pi/(3a_2), 0] \equiv \mathbf{K}_2$ with a_i being the original lattice constants. The K -points of the two layers differ from each other by $\Delta\mathbf{K} = \mathbf{K}_2 - \mathbf{K}_1$. A finite lattice mismatch ($a_1 \neq a_2$) or a possible relative twist angle θ between the layers yields $\Delta\mathbf{K} \neq 0$. This is illustrated in Fig. 10(a) in case of a finite twist angle. When the lattice mismatch and the twist angle is small, we have $|\Delta\mathbf{K}| \ll |\mathbf{K}_1|$. In this case, the interlayer tunneling leads to the hybridization between the low-energy electronic states of the two layers, separately in the K and K' -valleys. Correspondingly, the system acquires long-wavelength moiré pattern described by the moiré periodicity a_m and the reduced moiré Brillouin Zone (mBZ), see Fig. 10(a). Due to the large momentum mismatch between the original K and K' -valleys, the K -valley states do not hybridize with the K' -valley degrees of freedom and hence, as the TMD monolayers feature spin-valley locking due to the intrinsic spin-orbit coupling [6, 86], the valley index corresponds to the z -component of the spin. We can therefore consider the one-particle moiré Hamiltonian for each valley separately. We denote the valley-index as $\sigma \in \{\uparrow, \downarrow\}$, with

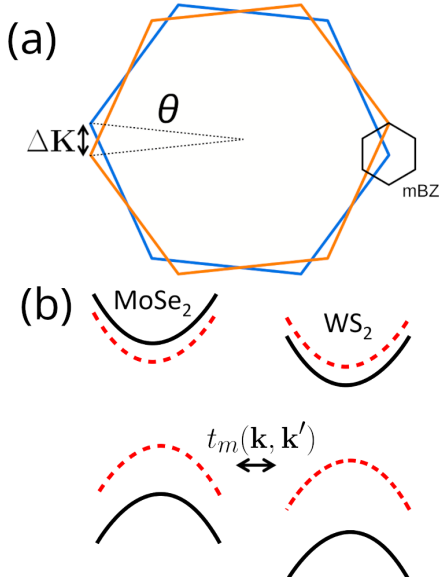


FIG. 10. (a) Schematic of the original BZ of the two layers forming the moiré lattice (blue and orange hexagons) as well as the moiré BZ (mBZ) of the K -valley. (b) Schematic picture of the highest valence and lowest conduction bands of the monolayer MoSe₂ and WS₂ at the K -valley. Dashed red (solid black) lines correspond to spin-down (spin-up) bands. The moiré potential arises due to a finite interlayer tunneling $t_m(\mathbf{k}, \mathbf{k}')$. In our analysis we only consider the highest valence band degrees of freedom.

$\sigma = \uparrow$ ($\sigma = \downarrow$) referring to the K -valley (K' -valley) and express the corresponding one-particle Hamiltonian as H_0^σ . We consider here only the K -valley electrons; the corresponding result for the K' -valley is obtained from the K -valley via time reversal.

The valence and conduction band dispersions of the decoupled MoSe₂ and WS₂ monolayers at the K -valley are shown schematically in Fig. 10(b). To a good approximation, these band structures can be taken to be parabolic. Furthermore, the valence and the conduction bands are separated by a large band gap. As it is common in experiments, we take the moiré system to be hole-doped within the highest valence band and hence we discard all the other bands. The highest valence bands of the two layers are coupled and the moiré pattern is formed due to the interlayer electron tunneling term $t_m(\mathbf{k}, \mathbf{k}') = t_m[\delta_{\mathbf{k}, \mathbf{k}'} + \delta_{\mathbf{k}-\mathbf{k}', \mathbf{b}_1^m} + \delta_{\mathbf{k}-\mathbf{k}', \mathbf{b}_2^m}]$ which describes a tunneling process from momentum state \mathbf{k}' to \mathbf{k} with \mathbf{b}_i^m being the basis vectors of the moiré reciprocal lattice [46, 87]. Consequently, the continuum Hamilto-

nian for the bi-layer reads

$$\begin{aligned}
 H_0^\dagger &= \sum_{\mathbf{k} \in \text{mBZ}} \Psi^\dagger(\mathbf{k}) \mathcal{H}(\mathbf{k}) \Psi(\mathbf{k}) \\
 \Psi(\mathbf{k}) &= [c_1(\mathbf{k}), c_2(\mathbf{k} - \Delta\mathbf{K})]^T \\
 [c_i(\mathbf{k})]_\alpha &= c_{i\uparrow}(\mathbf{k} + \mathbf{G}_\alpha) \\
 \mathcal{H}^\dagger(\mathbf{k}) &= \begin{bmatrix} \mathcal{H}_1^\dagger(\mathbf{k}) & \mathcal{H}_{12}^\dagger(\mathbf{k}) \\ [\mathcal{H}_{12}^\dagger(\mathbf{k})]^\dagger & \mathcal{H}_2^\dagger(\mathbf{k} - \Delta\mathbf{K}) \end{bmatrix} \quad (\text{B1})
 \end{aligned}$$

Here $c_{i\uparrow}(\mathbf{k})$ annihilates an electron within the highest valence band in valley $\sigma = \uparrow$ and layer i ($i = 1$ for MoSe₂ and $i = 2$ for WS₂). The reciprocal lattice vectors are $\mathbf{G}_\alpha \equiv n_\alpha \mathbf{b}_1^m + m_\alpha \mathbf{b}_2^m$ with n_α and m_α being integers. Moreover, $[\mathcal{H}_i^\dagger(\mathbf{k})]_{\alpha\beta} = \delta_{i,1} V - \delta_{\alpha\beta} \hbar^2 (\mathbf{k} + \mathbf{G}_\alpha)^2 / 2m_i$ contains the original parabolic dispersions for layer i with the effective mass m_i and the valence band edge off-set V between two layers. Finally, the off-diagonal block \mathcal{H}_{12}^\dagger describes the interlayer tunneling t_m between relevant momenta. For m_i and V we adopt the numerical values used in Ref. [46], i.e. $m_1 = 0.44m_e$, $m_2 = 0.32m_e$, $V = 270$ meV where m_e is the bare electron mass. The value used for t_m is discussed at the end of this section.

By diagonalizing the Hamiltonian (B1), one obtains the moiré band dispersion $\epsilon_{n\mathbf{k}}^\dagger$ such that

$$H_0^\dagger = \sum_{\mathbf{k} \in \text{mBZ}, n} \epsilon_{n\mathbf{k}}^\dagger \gamma_{n\mathbf{k}\uparrow}^\dagger \gamma_{n\mathbf{k}\uparrow} \quad (\text{B2})$$

Here $n = 1, 2, \dots$ is the moiré band index with $n = 1$ referring to the highest moiré valence band and $\gamma_{n\mathbf{k}\uparrow}$ are the corresponding moiré annihilation operators. In Fig. 2 the moiré dispersion $\epsilon_{n\mathbf{k}}^\dagger$ is shown for $\theta = 2.5^\circ$ computed with our parameters. The moiré hole band operators in Eq. (7) then read $h_{n\mathbf{k}\sigma}^\dagger = \gamma_{n-\mathbf{k}\sigma}$.

The diagonalization of H_0^\dagger yields the following transformation between the Bloch band basis and the original electron operators

$$\Psi_\uparrow(\mathbf{k}) = \begin{bmatrix} U_{\mathbf{k}\uparrow} \\ V_{\mathbf{k}\uparrow} \end{bmatrix} \gamma_\uparrow(\mathbf{k}) \equiv B_\uparrow(\mathbf{k}) \gamma_\uparrow(\mathbf{k}), \quad (\text{B3})$$

where $[\gamma_\uparrow(\mathbf{k})]_n = \gamma_{n\mathbf{k}\uparrow}$. Furthermore, the moiré Bloch states are stored as the column vectors of the unitary matrix $B_\uparrow(\mathbf{k})$ and its components $U_{\mathbf{k}\uparrow}$ and $V_{\mathbf{k}\uparrow}$ describe the projections to the two layers. Namely, the original electronic operators in the MoSe₂ layer can be expressed as $c_{1\uparrow}(\mathbf{k} + \mathbf{G}_\alpha) = \sum_{n=1} [U_{\mathbf{k}\uparrow}]_{\alpha n} \gamma_{n\mathbf{k}\uparrow}$. In other words, the Bloch functions in Eq. (7) are defined as $u_{n\sigma}(\mathbf{k} + \mathbf{G}_\alpha) \equiv [U_{\mathbf{k}\sigma}]_{\alpha n}$. Likewise, $V_{\mathbf{k}\uparrow}$ yields the projection to the WS₂ layer, i.e. $c_{2\uparrow}(\mathbf{k} + \mathbf{G}_\alpha) = \sum_{n=1} [V_{\mathbf{k}\uparrow}]_{\alpha n} \gamma_{n\mathbf{k}\uparrow}$.

As discussed in the main text, the highest moiré valence band can be described by the effective tight-binding Hamiltonian with appropriate Coulomb interaction terms, as written in Eq. (2). The hopping terms t_{ij}^σ are easy to obtain from the dispersion relation of the moiré band, i.e. one has $t_{ij}^\sigma = -\frac{1}{N} \sum_{\mathbf{k} \in \text{mBZ}} \epsilon_{1\mathbf{k}}^\sigma e^{-i\mathbf{k} \cdot (\mathbf{R}_i - \mathbf{R}_j)}$, where \mathbf{R}_i is the spatial coordinate of the i th moiré lattice site. To obtain the interaction terms, one needs appropriate expressions for the Coulomb interaction $V_C(\mathbf{q})$.

For the interlayer and intralayer interaction vertices we have in momentum space $V_{C,s}(q) = \frac{e^2}{2q\epsilon_s(q)} \tanh(qd_g)$, where $s = \perp$ ($s = \parallel$) stands for the interlayer (intralayer) interaction. We have furthermore taken into account the metallic gates, separated by a distance d_g from the moiré sample, which screen the Coulomb interactions via the hyperbolic tangent function [88]. The permittivities can be derived from the system geometry and in our case are given by $\frac{1}{\epsilon_{\parallel}(q)} = \frac{1+r^*q-r^*qe^{-2qd_l}}{\epsilon_0\epsilon_r[(1+r^*q)^2-(r^*q)^2e^{-2qd_l}]}$ and $\frac{1}{\epsilon_{\perp}(q)} = \frac{e^{-qd_l}}{\epsilon_0\epsilon_r[(1+r^*q)^2-(r^*q)^2e^{-2qd_l}]}$ [89]. Here ϵ_r is the average dielectric permittivity of the embedding material, r^* is the screening length of a TMD monolayer and d_l is the separation between two TMD layers. In our calculations we have chosen $\epsilon_r = 20$ due to the existence of the spacing and probe TMD layers. Moreover, we have $\epsilon_r r^* \sim 4$ nm [46], $d_l = 0.6$ nm and $d_g = 100$ nm.

Once the parameters for Eq. (2) are obtained, we can compute the parameters of the effective Heisenberg Hamiltonian for the half-filled moiré band by using the well-established strong coupling theory that maps the half-filled Fermi-Hubbard model to the Heisenberg model [90]. To this end, we employ the expressions given in the Supplementary Material of Ref. [14], i.e. $J_1 = -4X_{NN} + \frac{4t_{NN}^2}{U_0 - U_{NN}}$ and $J_2 = -4X_{NNN} + \frac{4t_{NNN}^2}{U_0 - U_{NNN}} + \frac{8t_{NN}^4}{U_0 - U_{NN}^3} \left(1 - \frac{U_0 - U_{NN}}{U_0 - U_{NNN}} + \frac{U_0 - U_{NN}}{2U_0 - 3U_{NN} + U_{NNN}}\right)$, where subscripts refer to NN or next-nearest-neighbour (NNN) terms. Note that these expressions for J_1 and J_2 assume real-valued hopping terms. As discussed in the main text, our analysis yields only a small imaginary part for t_{NN} , validating the use of the expressions of Ref. [14].

Coming back to choosing the interlayer tunneling parameter t_m , we note that the value given in Ref. [46], i.e. $t_m \sim 50$ meV, is too small in a sense that it yields $J \sim -0.06$ meV for the zero twist angle. However, in experiments [39] it has been shown that for the non-twisted and half-filled MoSe₂/WS₂, the magnetic order vanishes. This very likely happens due to the fact that the direct ferromagnetic exchange term X_{NN} cancels the antiferromagnetic super-exchange term in the expression of J_1 . To match this cancellation at $\theta = 0^\circ$, we use instead a value of $t_m \sim 90$ meV, which at $\theta = 0^\circ$ yields a vanishingly small J_1 . For larger twist angles used in our calculations, namely $\theta \in [2.6^\circ, 3.3^\circ]$, we find a positive J_1 , i.e. antiferromagnetic order. The fact that we need to fine-tune the parameters of the continuum model of Ref. [46] might imply that the predominant origin for the moiré potential of MoSe₂/WS₂ is not the inter-layer tunneling but the lattice reconstruction which could be addressed by using a continuum model with a one-particle long-wavelength moiré potential instead of an interlayer tunneling of Ref. [46]. This, however, does not affect the generality of our results as both the continuum models anyway lead to an effective triangular moiré lattice and because we study both antiferromagnetic and ferromagnetic in-plane orders.

Appendix C: Exciton-hole scattering

In this section, we derive the expression for the scattering matrix between an exciton in the mono-layer and a hole in the moiré system. To this end, we only consider the scattering between spin \uparrow excitons and spin \downarrow holes and discard the other scattering channel as its effect is negligible. Correspondingly, in the following discussion we suppress the spin index of the hole for a moment.

To simplify our analysis, we first consider a bilayer system of two TMD monolayers [50], shown in Fig. 11, where the exciton resides in layer A and a hole can tunnel between the layers A and B with the tunneling strength t . Therefore in case of our moiré setup, layer A corresponds to the probe TMD monolayer and layer B is the MoSe₂ monolayer of the moiré system. The Hamiltonian for the exciton and the hole is written in Eq. (II A). To a good approximation, the exciton-hole interaction $V(\mathbf{q})$ can be taken as a contact potential, i.e. $V(\mathbf{q}) = V$. Furthermore, layer A is biased by the potential energy Δ . Due to the finite tunneling term, one can diagonalize the one-particle Hamiltonian of the hole. The resulting eigenstates are called closed and open channels with energies $\epsilon_c(\mathbf{k}) = \epsilon_h(\mathbf{k}) + \Delta/2 + \sqrt{\frac{\Delta^2}{4} + t^2}$ and $\epsilon_o(\mathbf{k}) = \epsilon_h(\mathbf{k}) + \Delta/2 - \sqrt{\frac{\Delta^2}{4} + t^2}$. For later convenience, we write down the corresponding transformation between two hole bases as

$$\begin{aligned} \begin{bmatrix} a_{\mathbf{k}} \\ h_{\mathbf{k}} \end{bmatrix} &= \begin{bmatrix} \frac{x_c}{\sqrt{1+x_c^2}} & \frac{x_o}{\sqrt{1+x_o^2}} \\ \frac{1}{\sqrt{1+x_c^2}} & \frac{1}{\sqrt{1+x_o^2}} \end{bmatrix} \begin{bmatrix} h_{c\mathbf{k}} \\ h_{o\mathbf{k}} \end{bmatrix} \equiv U \begin{bmatrix} h_{c\mathbf{k}} \\ h_{o\mathbf{k}} \end{bmatrix} \\ &\equiv h(\mathbf{k}) = U \tilde{h}(\mathbf{k}) \text{ with,} \\ x_o &= \frac{\Delta}{2t} \left(1 - \sqrt{1 + \frac{4t^2}{\Delta^2}}\right) \\ x_c &= \frac{\Delta}{2t} \left(1 + \sqrt{1 + \frac{4t^2}{\Delta^2}}\right). \end{aligned} \quad (\text{C1})$$

Here $h_{c\mathbf{k}}$ and $h_{o\mathbf{k}}$ are the annihilation operators for the closed and open hole channels. Moreover, the columns of U are the corresponding eigenstates.

We proceed by writing down the \mathcal{T} -matrix between an exciton and hole. As we have two hole channels, the scattering matrix is a 2-by-2 matrix. It is straightforward to show that in the open and closed channel basis (tilde basis), it is

$$\tilde{\mathbf{T}}(\mathbf{k}, ik_n) = \begin{bmatrix} T_{oo}(\mathbf{k}, ik_n) & T_{oc}(\mathbf{k}, ik_n) \\ T_{co}(\mathbf{k}, ik_n) & T_{cc}(\mathbf{k}, ik_n) \end{bmatrix} = \frac{\tilde{\mathbf{V}}}{1 - \tilde{\mathbf{V}}\tilde{\mathbf{\Pi}}(\mathbf{k}, ik_n)}, \quad (\text{C2})$$

where the interaction matrix is $\tilde{\mathbf{V}} = U^\dagger \mathbf{V} U$ with $V_{ij} = V \delta_{i,j} \delta_{i,1}$ and the pair propagator $\tilde{\mathbf{\Pi}} = U^\dagger \mathbf{\Pi} U$. The tilded \mathbf{V} and $\mathbf{\Pi}$ are the interaction and pair propagator matrices in the original hole basis. From Eq. (C2), one can show that $\tilde{\mathbf{T}}(\mathbf{k}, ik_n) = U^\dagger \mathbf{T}(\mathbf{k}, ik_n) U$ with \mathbf{T} being

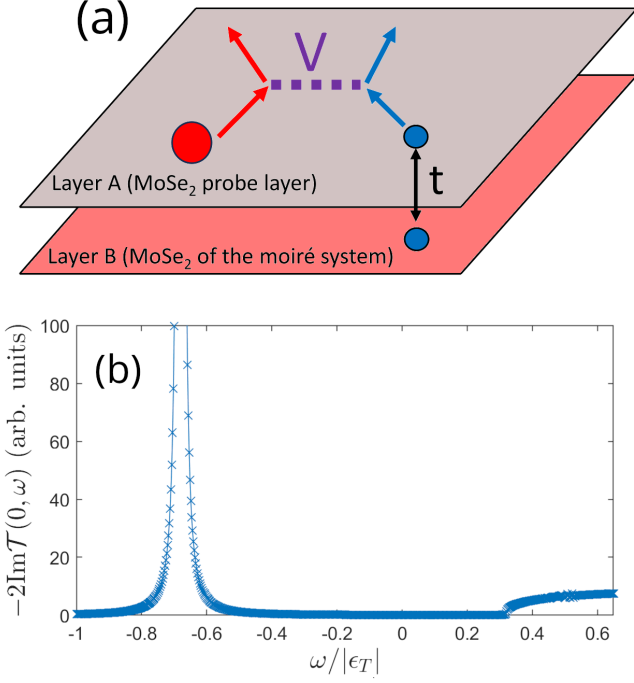


FIG. 11. (a) Schematic of the two-layer setup realising resonantly enhanced scattering between an exciton (red dot) in layer A and a hole (blue dots) in layer B [50]. The tunneling between the two layers is t and the interaction between the exciton and the hole is denoted as V . (b) Spectral function of the scattering matrix $\mathcal{T}(0, \omega)$ as a function of ω for $\Delta = \frac{8|\epsilon_T|}{25}$ with finite broadening $\eta = 0.0015|\epsilon_T|$.

the \mathcal{T} -matrix in the original basis such that

$$\mathbf{T}(\mathbf{k}, ik_n) = \begin{bmatrix} \mathcal{T}(\mathbf{k}, ik_n) & 0 \\ 0 & 0 \end{bmatrix} \quad (\text{C3})$$

$$\mathcal{T}(\mathbf{k}, ik_n) = \frac{V}{1 - V\Pi(\mathbf{k}, ik_n)} = \frac{1}{\Pi^{2B}(0, \epsilon_T) - \Pi(\mathbf{k}, ik_n)}, \quad (\text{C4})$$

where in the last step the contact interaction V is eliminated in the favor of the trion binding energy $\epsilon_T < 0$ and Π_{11}^{2B} is the vacuum pair propagator. Explicitly,

$$\Pi(0, z) = \frac{1}{A} \sum_{\mathbf{q}} \frac{1}{z + \Delta - q^2/2m_\mu} \quad (\text{C5})$$

$$\Pi^{2B}(0, \epsilon_T) = \frac{1}{A} \sum_{\mathbf{q}} \frac{1}{\epsilon_T + i\nu - q^2/2m_\mu} \quad (\text{C6})$$

where m_μ is the reduced mass of the exciton and hole. Trion bound state gives a rise to a pole for the \mathcal{T} -matrix. This can be seen in Fig. 11(b) where the zero-momentum spectral function of \mathcal{T} is plotted as a function of frequency ω . In addition to the pole at $\omega = \epsilon_T + \Delta$, the spectral function also features the usual scattering continuum at higher energies starting at $\omega = \Delta$. In the following, we discard the existence of the continuum as it appears in a non-relevant energy regime such that

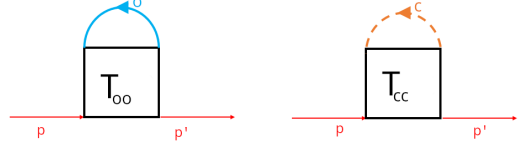


FIG. 12. Exciton self-energy diagrams to first order of the scattering matrix. Red lines depict exciton propagators and are not included in the self-energy. Blue solid (orange dashed) line correspond to the hole propagators in the closed (open) channel.

the \mathcal{T} -matrix can be written to as a pole expansion $\mathcal{T}(\mathbf{k}, z) = \frac{Z}{z - (\epsilon_T + \Delta + k^2/2m_T)}$, where m_T is the trion mass. In our calculations, we find that the residue Z is roughly momentum-independent such that $Z \approx 19 \frac{\hbar^2 |\epsilon_T|}{m_e}$, and correspondingly this is the value we used in all our computations.

Appendix D: Derivation of the exciton self-energies

In this section, we derive the expressions for the exciton self-energy terms Σ_1 and Σ_2 . We assume $t/\Delta \ll 1$, which is likely the experimental regime of interest as t is suppressed due to the spacing layer between the TMD monolayer and the moiré system. The hopping is desired to be small also because it otherwise would lead to hybridization between the moiré system and the TMD monolayer, and thus to the formation of one big three-layer moiré system. As we want to use the exciton in the TMD monolayer to probe the moiré system, this is not a desired scenario.

1. First order exciton self-energy Σ_1

The first order exciton self-energy Σ_1 in terms of open and closed channels is diagrammatically depicted in Fig. 12. Note that we have not fixed in-coming and out-going exciton momenta to be the same. Usually, they are the same but in our case, the hole in the moiré system feels the moiré potential which can lead to finite momentum kicks by the amount of moiré reciprocal lattice vectors \mathbf{G}_α . We therefore retain different incoming and outgoing exciton momenta, \mathbf{p} and \mathbf{p}' , for now and show below that $\mathbf{p}' = \mathbf{p} + \mathbf{G}_\alpha$.

As schematically presented in Fig. 12, Σ_1 consists of two terms corresponding to the exciton interacting with the closed and open channel holes, respectively. In the following, we ignore the closed channel contribution as we take it to be approximately empty. We therefore write

Σ_1 for imaginary time as

$$\begin{aligned} \Sigma_1(\mathbf{p}, \mathbf{p}', \tau_f - \tau_i) &= \frac{1}{A} \sum_{\mathbf{q}, \mathbf{q}'} T_{oo}(\mathbf{p} + \mathbf{q}, \tau_f - \tau_i) \\ &\times \langle -Th_o(\mathbf{q}, \tau_i) h_o^\dagger(\mathbf{q}', \tau_f) \rangle \delta_{\mathbf{p}', \mathbf{p} + \mathbf{q} - \mathbf{q}'}, \end{aligned} \quad (\text{D1})$$

where the Green's function for the open channel is $G_{oo}(\mathbf{q}, \mathbf{q}', \tau_i - \tau_f) = \langle -Th_{o\mathbf{q}}(\tau_i) h_{o\mathbf{q}'}^\dagger(\tau_f) \rangle$. In the limit of small t/Δ we obtain, up to the second order, the approximations $x_o \approx -\frac{t}{\Delta}$ and $x_c \approx \frac{\Delta}{t} \left(1 + \frac{t^2}{\Delta^2}\right)$. By using these, we get $|U_{12}|^2 \approx \frac{t^2}{\Delta^2}$, $|U_{22}|^2 \approx 1 - (t/\Delta)^2$, $U_{12}^* U_{22} \approx -t/\Delta$. For the self-energy Eq. (D1) we then obtain to the leading order of t^2/Δ^2

$$\begin{aligned} \Sigma_1(\mathbf{p}, \mathbf{p}', \tau_f - \tau_i) &\approx \frac{1}{A} \sum_{\mathbf{q}, \mathbf{q}'} \frac{t^2}{\Delta^2} \mathcal{T}(\mathbf{p} + \mathbf{q}, \tau_f - \tau_i) \\ &\times G(\mathbf{q}, \mathbf{q}', \tau_i - \tau_f) \delta_{\mathbf{p}', \mathbf{p} + \mathbf{q} - \mathbf{q}'}, \end{aligned} \quad (\text{D2})$$

where $G(\mathbf{q}, \mathbf{q}', \tau_i - \tau_f) = -\langle Th_{\mathbf{q}\downarrow}(\tau_i) h_{\mathbf{q}'\uparrow}^\dagger(\tau_f) \rangle$ is the Green's function for the holes in the MoSe₂ layer of the moiré system. Here we have re-introduced the spin index for the holes of the moiré system. From Eq. (D2) we see that Σ_1 can be expressed in the limit of small t^2/Δ^2 in terms of the Green's function of holes of the moiré system and the original exciton-hole \mathcal{T} -matrix. The tunneling between the moiré system and the exciton layer is taken into account with the multiplicative factor t^2/Δ^2 .

We project now the hole operators $h_{\mathbf{k}\downarrow}$ to the highest moiré valence band by writing

$$\begin{aligned} h_{-\mathbf{k}-\mathbf{G}_\alpha\sigma}^\dagger &= \sum_n [U_{\mathbf{k}\sigma}]_{\alpha n} \gamma_{n\mathbf{k}\sigma} \\ &\approx [U_{\mathbf{k}\sigma}]_{\alpha 1} \gamma_{1\mathbf{k}\sigma} \equiv u_\sigma(\mathbf{k} + \mathbf{G}_\alpha) \gamma_{1\mathbf{k}\sigma}, \end{aligned} \quad (\text{D3})$$

with $\mathbf{k} \in \text{mBZ}$. By furthermore transforming to real space via the Fourier transformation $\gamma_{1\mathbf{k}\sigma} = \frac{1}{\sqrt{N}} \sum_i e^{-i\mathbf{k}\cdot\mathbf{r}_i} h_{i\sigma}^\dagger$ with N being the number of moiré sites \mathbf{r}_i , we obtain

$$\Sigma_1(\mathbf{p}, \mathbf{p}', \tau) = \frac{t^2}{A\Delta^2} \sum_{\mathbf{q}, \mathbf{q}' \in \text{mBZ}} \sum_{\alpha\alpha'} \mathcal{T}(\mathbf{p} - \mathbf{q} - \mathbf{G}_\alpha, \tau) u_\downarrow^*(\mathbf{q} + \mathbf{G}_\alpha) u_\downarrow(\mathbf{q}' + \mathbf{G}_{\alpha'}) \sum_{ij} \frac{e^{i\mathbf{q}\cdot\mathbf{r}_i - i\mathbf{q}'\cdot\mathbf{r}_j}}{N} \langle -Th_{i\downarrow}(0) h_{j\downarrow}^\dagger(\tau) \rangle \delta_{\mathbf{p}', \mathbf{p} - \mathbf{q} + \mathbf{q}' - \mathbf{G}_\alpha + \mathbf{G}_{\alpha'}}. \quad (\text{D4})$$

We see that the Green's function inside the integrand of Eq. (D4) describes low-energy processes as $\langle -Th_{i-}(0) h_{j-}^\dagger(\tau) \rangle = \langle h_{j-}^\dagger(\tau) h_{i-}(0) \rangle$. This corresponds to the annihilation of a moiré hole instead of creating one (which would cost an energy of the on-site repulsion U_0). Therefore, in principle, Eq. (D4) should be solved such that the moiré hole operators h_i are expressed with the spinon and holon operators, in a similar manner as in Ref. [64]. This yields diagrams involving spin and holon propagators and a spin-holon bubble. Evaluating this bubble is outside the scope of the present work and we therefore use a simplified route, i.e. we assume we are far enough from the Feshbach resonance condition $\Delta = -\epsilon_T$ so that we can take the static limit of the \mathcal{T} -matrix, i.e. we write $\mathcal{T}(\mathbf{k}, \tau) \approx \mathcal{T}(\mathbf{k}) \delta(\tau)$ with $\mathcal{T}(\mathbf{k}) \equiv \mathcal{T}(\mathbf{k}, \omega = 0)$. From Eq. (D4) we then get

$$\Sigma_1(\mathbf{p}, \mathbf{p}', \tau) \approx \frac{1}{A} \frac{t^2}{\Delta^2} \delta(\tau) \sum_{\mathbf{q}, \mathbf{q}' \in \text{mBZ}} \sum_{\alpha\alpha'} \mathcal{T}(\mathbf{p} - \mathbf{q} - \mathbf{G}_\alpha) u_\downarrow^*(\mathbf{q} + \mathbf{G}_\alpha) u_\downarrow(\mathbf{q}' + \mathbf{G}_{\alpha'}) \frac{1}{N} \sum_{ij} e^{i\mathbf{q}\cdot\mathbf{r}_i} e^{-i\mathbf{q}'\cdot\mathbf{r}_j} \langle h_{j\downarrow}^\dagger h_{i\downarrow} \rangle \delta_{\mathbf{p}', \mathbf{p} - \mathbf{q} + \mathbf{q}' - \mathbf{G}_\alpha + \mathbf{G}_{\alpha'}}. \quad (\text{D5})$$

For the half-filled triangular moiré lattice we have $\langle h_{j\downarrow}^\dagger h_{i\downarrow} \rangle = \delta_{i,j} \left(\frac{1}{2} - \langle S_i^z \rangle\right)$. For the in-plane magnetism or spin liquids we have $\langle S_i^z \rangle = 0$ so we discard this term. Note that for the out-of-plane orders this term would be non-zero, therefore making it possible to detect out-of-plane magnetic order with Σ_1 , consistent with a recent mean-field proposal of Ref. [62]. For $\langle S_i^z \rangle = 0$, we however obtain

$$\begin{aligned} \Sigma_1(\mathbf{p}, \mathbf{p}', \tau) &\approx \frac{1}{2A} \frac{t^2}{\Delta^2} \delta(\tau) \sum_{\mathbf{q}, \mathbf{q}' \in \text{mBZ}} \sum_{\alpha\alpha'} \mathcal{T}(\mathbf{Q} - \mathbf{q} - \mathbf{G}_\alpha) u_\downarrow^*(\mathbf{q} + \mathbf{G}_\alpha) u_\downarrow(\mathbf{q}' + \mathbf{G}_{\alpha'}) \delta_{\mathbf{q}, \mathbf{q}'} \delta_{\mathbf{p}', \mathbf{p} - \mathbf{q} + \mathbf{q}' - \mathbf{G}_\alpha + \mathbf{G}_{\alpha'}} \\ &= \frac{1}{2A} \frac{t^2}{\Delta^2} \delta(\tau) \sum_{\mathbf{k}} \sum_{\lambda} \mathcal{T}(\mathbf{p} - \mathbf{k}) u_\downarrow^*(\mathbf{k}) u_\downarrow(\mathbf{k} + \mathbf{G}_\lambda) \delta_{\mathbf{p}', \mathbf{p} + \mathbf{G}_\lambda} \end{aligned} \quad (\text{D6})$$

where in the last line we have carried out a change of integration variables as $\mathbf{k} = \mathbf{q} + \mathbf{G}_\alpha$ and $\mathbf{G}_\lambda = \mathbf{G}_{\alpha'} - \mathbf{G}_\alpha$ such that the sum over \mathbf{k} is taken over the full momentum space, not just the moiré BZ. Finite terms for Σ_1 are

therefore

$$\Sigma_1(\mathbf{p}, \mathbf{p} + \mathbf{G}_\lambda, \tau) = \frac{1}{2A} \frac{t^2}{\Delta^2} \delta(\tau) \sum_{\mathbf{k}} \mathcal{T}(\mathbf{p} - \mathbf{k}) u_\downarrow^*(\mathbf{k}) u_\downarrow(\mathbf{k} + \mathbf{G}_\lambda) \quad (\text{D7})$$

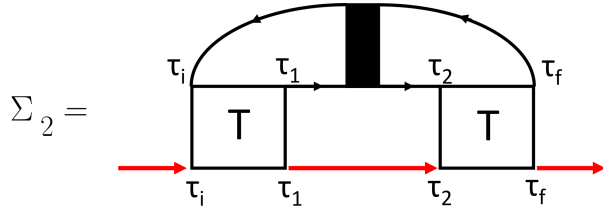


FIG. 13. The second order exciton self-energy Σ_2 in terms of the \mathcal{T} -matrix. Black box corresponds to the full two-particle propagator of moiré holes.

which is the Umklapp term discussed in the main text, i.e. the first term of Eq. (6). As noted in the main text, for the in-plane magnetism or spin liquid, this Umklapp term is not enough to obtain information about the in-plane magnetic correlations within the system.

To get the estimate for the zero-momentum energy shift due to the Umklapp potential, i.e. δE_{Um} , we consider Eq. (D7) with $\mathbf{p} = 0$ and $\mathbf{G}_\lambda = 0$, such that we have

$$\delta E_{\text{Um}} = \frac{t^2}{2A\Delta^2} \sum_{\mathbf{k}} \mathcal{T}(\mathbf{k}) |u_\downarrow(\mathbf{k})|^2 = \frac{t^2 Z}{\Delta^2 a_m^2} \beta, \quad (\text{D8})$$

where β is the \mathbf{k} -integral in dimensionless units, i.e. $\beta = \frac{1}{8\pi^2} \int d\tilde{\mathbf{k}} \frac{|u_\downarrow(\tilde{\mathbf{k}})|^2}{1 - \Delta - \alpha_r k^2}$ with $\alpha_r = 1/(|\epsilon_T| 2m_T a_m^2)$ and tilded variables are dimensionless. As $\beta \sim \mathcal{O}(1)$, we have $\delta E_{\text{Um}} \sim \mathcal{O}(\frac{t^2 Z}{\Delta^2 a_m^2})$.

2. Second order exciton self-energy Σ_2 and the spin-spin correlator

After having calculated the Umklapp contribution arising from Σ_1 , we consider another type of exciton self-energy depicted in Fig. 13, which we denote Σ_2 . This self-energy is second order in the \mathcal{T} -matrix and contains information about the dynamical spin-spin correlations of the holes in the moiré lattice.

We can write Σ_2 in imaginary time to leading order in t^4/Δ^4 as

$$\Sigma_2(\mathbf{p}, \mathbf{p}', \tau = \tau_f - \tau_i) = \frac{t^4}{\Delta^4 A^2} \sum_{\mathbf{q}} \int_0^\beta d\tau_1 \int_0^\beta d\tau_2 \mathcal{G}(\mathbf{p} + \mathbf{q}, \tau_2 - \tau_1) \sum_{\mathbf{k}\mathbf{k}'} \mathcal{T}(\mathbf{p} + \mathbf{k} + \mathbf{q}, \tau - \tau_i) \mathcal{T}(\mathbf{p} + \mathbf{k}' + \mathbf{q}, \tau_f - \tau_2) \times \langle h_{\mathbf{k}'+\mathbf{q}\downarrow}^\dagger(\tau_f) h_{\mathbf{k}'\downarrow}(\tau_2) h_{\mathbf{k}\downarrow}^\dagger(\tau_1) h_{\mathbf{k}+\mathbf{q}\downarrow}(\tau_i) \rangle \delta_{\mathbf{p}', \mathbf{p}+\mathbf{q}-\mathbf{q}'}. \quad (\text{D9})$$

As in case of Σ_1 , we again assume that we are sufficiently far away from the Feshbach resonance such that we can approximate the \mathcal{T} -matrix with its static limit, i.e. $\mathcal{T}(\mathbf{k}, \tau) \approx \mathcal{T}(\mathbf{k}) \delta(\tau)$. We can then cast Eq. (D9) as

$$\Sigma_2(\mathbf{p}, \mathbf{p}', \tau) \approx \frac{t^4}{\Delta^4 A^2} \sum_{\mathbf{q}} \mathcal{G}(\mathbf{p} + \mathbf{q}, \tau) \sum_{\mathbf{k}\mathbf{k}'} \mathcal{T}(\mathbf{p} + \mathbf{k} + \mathbf{q}) \mathcal{T}(\mathbf{p} + \mathbf{k}' + \mathbf{q}) \langle h_{\mathbf{k}'+\mathbf{q}\downarrow}^\dagger(\tau) h_{\mathbf{k}'\downarrow}(\tau) h_{\mathbf{k}\downarrow}^\dagger h_{\mathbf{k}+\mathbf{q}\downarrow} \rangle \delta_{\mathbf{p}', \mathbf{p}+\mathbf{q}-\mathbf{q}'}. \quad (\text{D10})$$

We proceed now the same way as before, i.e. project $h_{\mathbf{k}\downarrow}$ to the highest moiré valence band with Eq. (D3) and transform to the real space of the moiré lattice. This gives

$$\Sigma_2(\mathbf{p}, \mathbf{p}', \tau) \approx \frac{t^4}{\Delta^4 A^2} \sum_{\mathbf{q}\mathbf{q}' \in \text{mBZ}} \sum_{\lambda\lambda'} \mathcal{G}(\mathbf{p} - \mathbf{q} - \mathbf{G}_\lambda, \tau) \sum_{\mathbf{k}\mathbf{k}' \in \text{mBZ}} \sum_{\alpha\beta} \mathcal{T}(\mathbf{p} - \mathbf{k} - \mathbf{G}_\alpha - \mathbf{q} - \mathbf{G}_\lambda) \mathcal{T}(\mathbf{p} - \mathbf{k}' - \mathbf{G}_\beta - \mathbf{q} - \mathbf{G}_\lambda) \times u_\downarrow(\mathbf{k}' + \mathbf{q}' + \mathbf{G}_\beta + \mathbf{G}_{\lambda'}) u_\downarrow^*(\mathbf{k}' + \mathbf{G}_\beta) u_\downarrow(\mathbf{k} + \mathbf{G}_\alpha) u_\downarrow^*(\mathbf{k} + \mathbf{G}_\alpha + \mathbf{q} + \mathbf{G}_\lambda) \delta_{\mathbf{p}', \mathbf{p}-\mathbf{q}-\mathbf{G}_\lambda+\mathbf{q}'+\mathbf{G}_{\lambda'}} \times \frac{1}{N} \sum_{i,i',i'',i'''} e^{-i(\mathbf{q}'+\mathbf{k}') \cdot \mathbf{r}_i} e^{i\mathbf{k}' \cdot \mathbf{r}_{i'}} e^{-i\mathbf{k} \cdot \mathbf{r}_{i''}} e^{i(\mathbf{q}+\mathbf{k}) \cdot \mathbf{r}_{i'''}} \langle T h_{i\downarrow}^\dagger(\tau) h_{i'\downarrow}(\tau) h_{i''\downarrow}^\dagger h_{i'''\downarrow} \rangle. \quad (\text{D11})$$

By focusing on the last line, one can see that if $i'' \neq i'''$ or $i \neq i'$, the term $\langle T h_{i\downarrow}^\dagger(\tau) h_{i'\downarrow}(\tau) h_{i''\downarrow}^\dagger h_{i'''\downarrow} \rangle$ is proportional to $e^{\tau U_0}$. Later, when transforming to Matsubara frequencies, this quickly oscillating term suppresses the self-energy by a factor of $1/U_0$. As the repulsive interaction U_0 is the dominant energy scale in our lattice model, we can ignore such non-local terms with $i'' \neq i'''$ or $i \neq i'$ and instead take $i' = i$ and $i''' = i'' \equiv j$. Hence, we get

$$\Sigma_2(\mathbf{p}, \mathbf{p}', \tau) \approx \frac{t^4}{\Delta^4 A^2} \sum_{\mathbf{q}\mathbf{q}' \in \text{mBZ}} \sum_{\lambda\lambda'} \mathcal{G}(\mathbf{p} - \mathbf{q} - \mathbf{G}_\lambda, \tau) \sum_{\mathbf{k}\mathbf{k}' \in \text{mBZ}} \sum_{\alpha\beta} \mathcal{T}(\mathbf{p} - \mathbf{k} - \mathbf{G}_\alpha - \mathbf{q} - \mathbf{G}_\lambda) \mathcal{T}(\mathbf{p} - \mathbf{k}' - \mathbf{G}_\beta - \mathbf{q} - \mathbf{G}_\lambda) \times u_\downarrow(\mathbf{k}' + \mathbf{q}' + \mathbf{G}_\beta + \mathbf{G}_{\lambda'}) u_\downarrow^*(\mathbf{k}' + \mathbf{G}_\beta) u_\downarrow(\mathbf{k} + \mathbf{G}_\alpha) u_\downarrow^*(\mathbf{k} + \mathbf{G}_\alpha + \mathbf{q} + \mathbf{G}_\lambda) \delta_{\mathbf{p}', \mathbf{p}-\mathbf{q}-\mathbf{G}_\lambda+\mathbf{q}'+\mathbf{G}_{\lambda'}} \times \frac{1}{N} \sum_{ij} e^{-i\mathbf{q}' \cdot \mathbf{r}_i} e^{i\mathbf{q} \cdot \mathbf{r}_j} \langle T h_{i\downarrow}^\dagger(\tau) h_{i\downarrow}(\tau) h_{j\downarrow}^\dagger h_{j\downarrow} \rangle. \quad (\text{D12})$$

This can be further simplified at half-filling by noting that $h_{i\downarrow}^\dagger h_{i\downarrow} = \frac{1}{2} - S_i^z$. By inserting this to Eq. (D12) and further transferring to Matsubara frequency space, we obtain

$$\begin{aligned} \Sigma_2(\mathbf{p}, \mathbf{p}', i\omega_n) &= \frac{1}{N\beta} \frac{t^4}{\Delta^4} \frac{1}{A^2} \sum_{\mathbf{q}\mathbf{q}' \in \text{mBZ}} \sum_{\lambda\lambda'} \sum_{iq_n} \mathcal{G}(\mathbf{p} - \mathbf{q} - \mathbf{G}_\lambda, i\omega_n + iq_n) \delta_{\mathbf{p}', \mathbf{p} - \mathbf{q} - \mathbf{G}_\lambda + \mathbf{q}' + \mathbf{G}_{\lambda'}} \\ &\times \left[\sum_{\mathbf{k}} \mathcal{T}(\mathbf{p} - \mathbf{k} - \mathbf{q} - \mathbf{G}_\lambda) U_-(\mathbf{k}) U_-^*(\mathbf{k} + \mathbf{q} + \mathbf{G}_\lambda) \right] \left[\sum_{\mathbf{k}'} \mathcal{T}(\mathbf{p} - \mathbf{k}' - \mathbf{q} - \mathbf{G}_\lambda) U_-^*(\mathbf{k}') U_-(\mathbf{k}' + \mathbf{q}' + \mathbf{G}_{\lambda'}) \right] \\ &\times \int_0^\beta d\tau e^{-iq_n\tau} \langle T S_{\mathbf{q}'}^z(\tau) S_{-\mathbf{q}}^z \rangle. \end{aligned} \quad (\text{D13})$$

Here we have discarded reducible diagrams. One should note that the sums of \mathbf{k} and \mathbf{p} are taken over the whole momentum space. The last line in Eq. (D13) is the spin-spin correlator. If we assume the translational invariance for the spin-spin correlator (which should hold for a 120° AFM, FM, or a spin liquid), i.e. that $\langle S_{j+\Delta j}^z(\tau) S_j^z \rangle$ depends only on the relative distance Δj between two lattice sites j and $j + \Delta j$, we find $\mathbf{q}' = \mathbf{q}$ such that

$$\begin{aligned} \Sigma_2(\mathbf{p}, \mathbf{p}', i\omega_n) &= \frac{1}{N\beta} \frac{t^4}{\Delta^4} \frac{1}{A^2} \sum_{\mathbf{q} \in \text{mBZ}} \sum_{\lambda\lambda'} \sum_{iq_n} \mathcal{G}(\mathbf{p} - \mathbf{q} - \mathbf{G}_\lambda, i\omega_n + iq_n) \chi_{zz}(\mathbf{q}, -iq_n) \delta_{\mathbf{p}', \mathbf{p} - \mathbf{G}_\lambda + \mathbf{G}_{\lambda'}} \\ &\times \left[\sum_{\mathbf{k}} \mathcal{T}(\mathbf{p} - \mathbf{k} - \mathbf{q} - \mathbf{G}_\lambda) u_{\downarrow}(\mathbf{k}) u_{\downarrow}^*(\mathbf{k} + \mathbf{q} + \mathbf{G}_\lambda) \right] \left[\sum_{\mathbf{k}'} \mathcal{T}(\mathbf{p} - \mathbf{k}' - \mathbf{q} - \mathbf{G}_\lambda) u_{\downarrow}^*(\mathbf{k}') u_{\downarrow}(\mathbf{k}' + \mathbf{q} + \mathbf{G}_{\lambda'}) \right] \end{aligned} \quad (\text{D14})$$

where the spin-spin correlator is $\chi_{zz}(\mathbf{q}, iq_n) = \int_0^\beta d\tau e^{iq_n\tau} \langle T S_{\mathbf{q}}^z(\tau) S_{-\mathbf{q}}^z \rangle$. By defining a new label as $\mathbf{G}_\alpha = \mathbf{G}_{\lambda'} - \mathbf{G}_\lambda$ we get

$$\begin{aligned} \Sigma_2(\mathbf{p}, \mathbf{p} + \mathbf{G}_\alpha, i\omega_n) &= \frac{1}{N\beta} \frac{t^4}{\Delta^4} \frac{1}{A^2} \sum_{\mathbf{q} \in \text{mBZ}} \sum_{\lambda} \sum_{iq_n} \mathcal{G}(\mathbf{p} - \mathbf{q} - \mathbf{G}_\lambda, i\omega_n + iq_n) \chi_{zz}(\mathbf{q}, -iq_n) \\ &\times \left[\sum_{\mathbf{k}} \mathcal{T}(\mathbf{p} - \mathbf{k} - \mathbf{q} - \mathbf{G}_\lambda) u_{\downarrow}(\mathbf{k}) u_{\downarrow}^*(\mathbf{k} + \mathbf{q} + \mathbf{G}_\lambda) \right] \left[\sum_{\mathbf{k}'} \mathcal{T}(\mathbf{p} - \mathbf{k}' - \mathbf{q} - \mathbf{G}_\lambda) u_{\downarrow}^*(\mathbf{k}') u_{\downarrow}(\mathbf{k}' + \mathbf{q} + \mathbf{G}_\lambda + \mathbf{G}_\alpha) \right]. \end{aligned} \quad (\text{D15})$$

We can express this as

$$\Sigma_2(\mathbf{p}, \mathbf{p} + \mathbf{G}_\alpha, i\omega_n) = \frac{1}{N\beta} \frac{t^4}{\Delta^4} \frac{1}{A^2} \sum_{\mathbf{q}} \sum_{iq_n} \mathcal{G}(\mathbf{p} - \mathbf{q}, i\omega_n - iq_n) \chi_{zz}(\mathbf{q}, iq_n) g(\mathbf{p}, -\mathbf{q}) g(\mathbf{p} - \mathbf{q}, \mathbf{q} + \mathbf{G}_\alpha), \quad (\text{D16})$$

$$g(\mathbf{p}, \mathbf{q}) = \sum_{\mathbf{k}} \mathcal{T}(\mathbf{p} - \mathbf{k} + \mathbf{q}) u_{\downarrow}(\mathbf{k}) u_{\downarrow}^*(\mathbf{k} - \mathbf{q}), \quad (\text{D17})$$

which is the same expression as in the main text.

We have therefore obtained the Umklapp self-energy term of Eq. (D7) and the term containing the spin-spin correlator given by Eq. (D17). The major approximation to derive these terms was to take the static limit of the exciton-hole \mathcal{T} -matrix. If one wanted to take into account the full frequency dependency of the \mathcal{T} -matrices, evaluating the diagram of Fig. 13 would be very challenging as it would contain a two-particle Green's function that would split into complicated spinon-holon correlators. We leave this topic for future studies.

Appendix E: Additional details concerning computing Σ_2 with SCBA

In this section, we provide further practical details regarding our SCBA computations to evaluate Eq. (8). To this end, it is convenient to write Σ_2 by folding the exciton dispersion to the mBZ such that Σ_2 reads

$$[\Sigma_2(\mathbf{p}, ip_n)]_{nn'} = \frac{1}{\beta N} \sum_{\substack{\mathbf{q} \in \text{mBZ} \\ iq_n}} \chi_{zz}(q) [\tilde{W}^\dagger(\mathbf{p}, \mathbf{q}) \mathcal{G}(\mathbf{p} + \mathbf{q}, ip_n + iq_n) \tilde{W}(\mathbf{p}, \mathbf{q})]_{nn'} \quad (\text{E1})$$

with

$$\tilde{W}_{nm}(\mathbf{p}, \mathbf{q}) \equiv \frac{1}{A} \sum_{\mathbf{k}, \alpha\lambda} \mathcal{T}(\mathbf{p} + \mathbf{G}_\alpha - \mathbf{k}) S_n^*(\mathbf{p} + \mathbf{G}_\alpha + \mathbf{q} + \mathbf{G}_\lambda) S_m(\mathbf{p} + \mathbf{G}_\alpha) U_\sigma(\mathbf{k} + \mathbf{q} + \mathbf{G}_\lambda) U_\sigma^*(\mathbf{k}), \quad (\text{E2})$$

where we have expressed the exciton degrees of freedom in the eigenbasis of the Umklapp potential, i.e. $X_{\mathbf{p}+\mathbf{G}_\alpha} = \sum_n S_n(\mathbf{p} + \mathbf{G}_\alpha) \gamma_{X_n}(\mathbf{p})$. Here, $S_n(\mathbf{p})$ are the Bloch functions of the excitons and $\gamma_{X_n}(\mathbf{p})$ are the exciton annihilation

operators for exciton bands n and momenta \mathbf{p} , corresponding to exciton energies $\epsilon_{X_n}(\mathbf{p})$. Moreover, the excitonic Green's function $\mathcal{G}(Q)$ in the new basis reads $[\mathcal{G}(\mathbf{p}, \tau)]_{nm} = -\langle T\gamma_{X_n}(\mathbf{p}, \tau)\gamma_{X_m}^\dagger(\mathbf{p}) \rangle$ such that $\mathcal{G}_X^{-1}(Q) = \mathcal{G}_0^{-1}(p) - \Sigma_2(p)$ and $[\mathcal{G}_0^{-1}(p)]_{nm} = \delta_{nm}[ip_n - \epsilon_{X_n}(\mathbf{p})]$ with the notation $p = (\mathbf{p}, ip_n)$.

By using the LSWT result for the spin-spin correlator χ_{zz} and the fact that we are considering a single exciton, we can carry out the Matsubara sum in Eq. (E1) giving at zero temperature

$$[\Sigma_2(\mathbf{p}, \omega)]_{nn'} = \frac{1}{N} \sum_{\mathbf{q} \in \text{mBZ}} (2u_{\mathbf{q}}v_{\mathbf{q}} - (u_{\mathbf{q}}^2 + v_{\mathbf{q}}^2)) [\tilde{W}^\dagger(\mathbf{p}, \mathbf{q})\mathcal{G}(\mathbf{p} + \mathbf{q}, \omega + 0^+ - \epsilon_{\mathbf{q}})\tilde{W}(\mathbf{p}, \mathbf{q})]_{nn'}. \quad (\text{E3})$$

As the exciton Green's function \mathcal{G} at the right hand side of Eq. (E3) depends on the self-energy Σ_2 , Eq. (E3) needs to be solved self-consistently. To this end, we used an initial ansatz $\mathcal{G} = \mathcal{G}_0$ and solved Eq. (E3) iteratively by computing a new value for Σ_2 with Eq. (E3) which was then used to obtain a new \mathcal{G} via $\mathcal{G}^{-1} = \mathcal{G}_0^{-1} - \Sigma_2$. This procedure was repeated until Σ_2 converged to a stable solution. Note that the second order perturbation results of Fig. 16 are obtained by terminating this loop after the first iteration, see Sec. G. As the term arising from the coherence factors of the spin wave excitations is strongly peaked around the Dirac points in case of the AFM, we used non-uniform grid with more momentum points around the Dirac points to evaluate the momentum integral of Eq. (E3).

We see from Eq. (E3) that in general the exciton self-energy and the Green's function \mathcal{G} are matrices expressed in the exciton band basis. This representation arises when we folded the dispersion of the free exciton to the moiré BZ. This is an alternative presentation to Eq. (D16) where the exciton self-energy and the Green's function are expressed in terms of the moiré reciprocal vectors \mathbf{G}_α . The expressions in the main text are for simplicity presented in terms of \mathbf{G}_α and the results of the main text are obtained from Eq. (E3) by considering only the lowest exciton band, i.e. $n = 1$. We have numerically checked that by including the second band has a negligible effect on our results.

In the main text, numerical results are shown along the Γ - M path in the mBZ. For completeness, in Fig. 14 the spectral function is shown along the Γ - K - K' - Γ path. We see that the spectral features are similar those in Fig. 7, i.e. there is a clear low energy quasiparticle peak from the exciton-polaron state and broader peaks at higher energies corresponding to geometric string excitations.

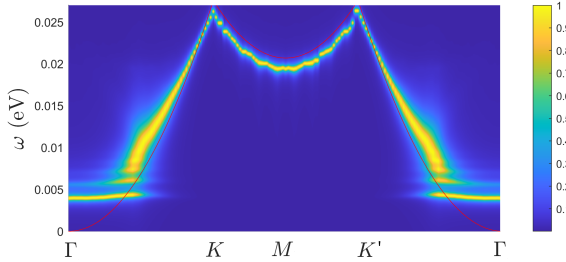


FIG. 14. Exciton spectral function $A(\mathbf{p}, \omega)$ for the twist angle $\theta = 3^\circ$ and an in-plane AFM along the Γ - K - K' - Γ path within the mBZ as a function of the momentum and energy. The red solid line gives the bare exciton dispersion.

Appendix F: Physical picture for the presence of string excitations

In this section, we give elaborate on the physical reason why the string excitations are present in case of the AFM but not for the FM. We start by noting that after approximating the exciton-hole \mathcal{T} -matrix with its static limit, the effective exciton-hole interaction Hamiltonian

for the lowest exciton band reads

$$H_{X-h} = \sum_{\mathbf{p}, \mathbf{q} \in \{\text{mBZ}\}} V(\mathbf{p}, \mathbf{q}) \gamma_{\mathbf{p}+\mathbf{q}}^\dagger \gamma_{\mathbf{p}} s_{\mathbf{q}}^z, \quad (\text{F1})$$

with

$$V(\mathbf{p}, \mathbf{q}) = \frac{1}{\sqrt{NA}} \tilde{W}_{11}(\mathbf{p}, \mathbf{q}) \quad (\text{F2})$$

where $\gamma_{\mathbf{p}} \equiv \gamma_{X_1}(\mathbf{p})$ is the exciton annihilation operator for the lowest exciton band (See the previous section for the notation). In other words, the exciton can scatter by creating a spin flip in the moiré system. This is due to the fact that for the in-plane magnetic order, s_i^z flips the spin of moiré site i . By Fourier transforming Eq. (F1) to real space of moiré sites h_i and exciton sites $\gamma_i = \frac{1}{\sqrt{N}} \sum_{\mathbf{p}} e^{i\mathbf{p}\cdot\mathbf{r}_i} \gamma_{\mathbf{p}}$, one finds

$$H_{X-h} = \sum_{i, i', j'} V(\mathbf{r}_{i'} - \mathbf{r}_{j'}, \mathbf{r}_i - \mathbf{r}_i) \gamma_{i'}^\dagger \gamma_j s_i^z. \quad (\text{F3})$$

We therefore see explicitly that the exciton hopping can create spin flips, analogous to a hole hopping in a AFM lattice. We have numerically checked that $V(\mathbf{r}_1, \mathbf{r}_2)$ is largest for the local processes, i.e. $\mathbf{r}_{i'} = \mathbf{r}_{j'} = \mathbf{r}_i$, such that the exciton mainly creates spin flips at the nearest moiré site. It follows that when the exciton moves around, it creates spin flips in its wake. In other words, spin flips take place in the proximity of the exciton and hence the exciton can become dressed due to the cloud of spin flips around it.

We see that in Eq. (F3) there exists also non-local hopping terms for the exciton. These are not included in the heuristic picture acquired from Eq. (4) and discussed in Sec. III A. Indeed, we have numerically checked that such

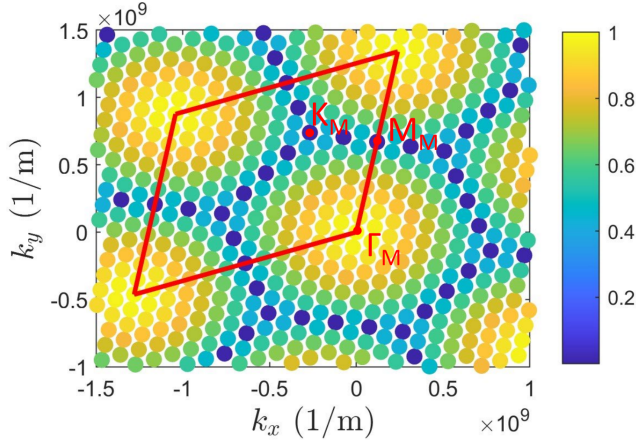


FIG. 15. $V(0, \mathbf{q})/\max[V(0, \mathbf{q})]$ in Eq. (F2) as a function of momentum \mathbf{q} for $\theta = 2.6^\circ$. Red parallelogram indicates the momentum space unit cell.

hopping terms given by Eq. (F3) are much smaller in amplitude compared to the dominant local term. The reason for the existence of non-local terms lies in the fact that Eq. (F3) is obtained by projecting the hole (exciton) operators to the highest moiré valence band (lowest exciton band). Such a projection scheme yields the interaction vertex $V(\mathbf{p}, \mathbf{q})$ of Eq. (F1) that depends on the momenta of both exciton and hole. This is in contrast to the original exciton-hole \mathcal{T} -matrix of Eq. (4) that depends only on the total center-of-mass momentum.

It is now illuminating to consider again the momentum-space representation of Eq. (F1). As can be seen in Fig. 7, string excitations take place for small exciton momentum \mathbf{p} . Motivated by this observation, we consider $\mathbf{p} = 0$ and correspondingly in Fig. 15 show $V(0, \mathbf{q})$ as a function of the spin wave momentum \mathbf{q} . From Fig. 15 we see that the creation of spin wave excitations is most prominent for small momenta \mathbf{q} . Therefore, string excitations are present (absent) for the AFM (FM) order as local spin flips, that preserve their shape and compactness, can (cannot) be constructed from the linearly (quadratically) dispersing spin wave excitations near $\mathbf{q} = 0$.

Appendix G: Second order perturbation theory

To demonstrate that the non-perturbative SCBA is required to reveal the string excitations, in Fig. 16 we show the exciton spectral weight for $\theta = 3^\circ$ as a function of momentum and frequency obtained with the non-self-consistent second order perturbation theory by excluding the contribution of Σ_2 within the integrand of Eq. (8),

i.e. by using the non-interacting exciton Green's function

$$\mathcal{G}^{-1}(\mathbf{p}', \mathbf{p}, i\omega_n) = i\omega_n - \epsilon_{\mathbf{p}}^x - \Sigma_1(\mathbf{p}', \mathbf{p}) \quad (\text{G1})$$

in Eq. (8). We see that the string excitations are absent in Fig. 16 as compared to the SCBA results shown in Fig. 7,

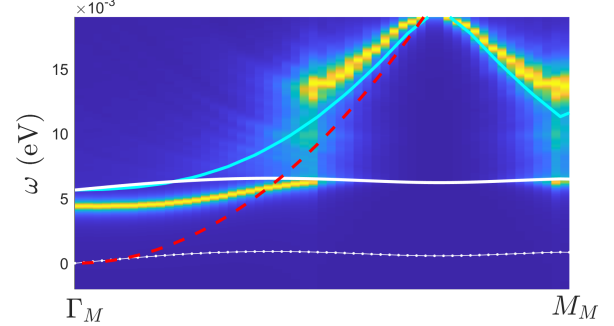


FIG. 16. Exciton spectral weight $A(\mathbf{p}, \omega)$ at $\theta = 3^\circ$ as a function of the frequency and the momentum obtained with the non-self-consistent second order perturbation theory. Red dashed, solid cyan, das-dotted white and solid white lines correspond, respectively, to the bare exciton dispersion, exciton dispersion in the presence of the Umklapp potential Σ_1 , spin wave spectrum and ω_c (see text for meaning of ω_c). These results should be compared to the corresponding SCBA results of Fig. 7. We see that the string excitations are absent, highlighting the importance of our SCBA approach.

underscoring the importance of the non-perturbative SCBA to describe the spectral properties of the probe exciton correctly.

Both the second order results of Fig. 16 and the results of the SCBA computations shown in Fig. 7 reveal that a well-defined quasi-particle exists only for small momenta, and that it is strongly damped elsewhere in the mBZ, although they disagree concerning its energy. To explain the damping within the second order perturbation theory, we consider the integrand of Eq. (6) with Eq. (G1) and $\mathbf{p}' = \mathbf{p}$ and note that $\epsilon_{\mathbf{p}}^x + \Sigma_1(\mathbf{p}, \mathbf{p}) \sim \delta E_{Um} + p^2/(2m_{Um})$. Here δE_{Um} (m_{Um}) is the zero-momentum energy shift (effective mass) of the exciton due to the Umklapp potential. From Eq. (8) we can deduce that the particle-hole scattering continuum should for a given momentum \mathbf{p} start at the critical frequency $\omega_c(\mathbf{p}) = \min_{\mathbf{q}}[\omega_{\mathbf{q}} + \delta E_{Um} + (\mathbf{p} - \mathbf{q})^2/(2m_{Um})]$. As the spin wave dispersion $\omega_{\mathbf{q}}$ remains rather flat compared to the exciton energies, for large enough \mathbf{p} this condition yields $\omega_c(\mathbf{p}) = \delta E_{Um} + \omega_{\mathbf{p}}$. In Fig. 16 we have plotted this estimate as a white line. We see that once the energy of the well-defined quasi-particle mode crosses this condition, it becomes damped. Hence, the condition for ω_c explains the damping of the exciton-polaron mode. Similar damping and the transfer of the spectral weight from the quasi-particle mode to the excited states and broad continuum are also seen in case of the strong coupling SCBA results of Fig. 7.

- [1] D. Xiao, G.-B. Liu, W. Feng, X. Xu, and W. Yao, Coupled spin and valley physics in monolayers of mos_2 and other group-vi dichalcogenides, *Phys. Rev. Lett.* **108**, 196802 (2012).
- [2] T. Cao, G. Wang, W. Han, H. Ye, C. Zhu, J. Shi, Q. Niu, P. Tan, E. Wang, B. Liu, and J. Feng, Valley-selective circular dichroism of monolayer molybdenum disulphide, *Nature Communications* **3**, 887 EP (2012), article.
- [3] H. Zeng, J. Dai, W. Yao, D. Xiao, and X. Cui, Valley polarization in mos_2 monolayers by optical pumping, *Nature Nanotechnology* **7**, 490 (2012).
- [4] K. F. Mak, K. He, J. Shan, and T. F. Heinz, Control of valley polarization in monolayer mos_2 by optical helicity, *Nature Nanotechnology* **7**, 494 (2012).
- [5] J. R. Schaibley, H. Yu, G. Clark, P. Rivera, J. S. Ross, K. L. Seyler, W. Yao, and X. Xu, Valleytronics in 2d materials, *Nature Reviews Materials* **1**, 16055 EP (2016), review Article.
- [6] G. Wang, A. Chernikov, M. M. Glazov, T. F. Heinz, X. Marie, T. Amand, and B. Urbaszek, Colloquium: Excitons in atomically thin transition metal dichalcogenides, *Rev. Mod. Phys.* **90**, 021001 (2018).
- [7] L. Balents, C. R. Dean, D. K. Efetov, and A. F. Young, Superconductivity and strong correlations in moiré flat bands, *Nature Physics* **16**, 725 (2020).
- [8] D. M. Kennes, M. Claassen, L. Xian, A. Georges, A. J. Millis, J. Hone, C. R. Dean, D. N. Basov, A. N. Pasupathy, and A. Rubio, Moiré heterostructures as a condensed-matter quantum simulator, *Nature Physics* **17**, 155 (2021).
- [9] E. Y. Andrei, D. K. Efetov, P. Jarillo-Herrero, A. H. MacDonald, K. F. Mak, T. Senthil, E. Tutuc, A. Yazdani, and A. F. Young, The marvels of moiré materials, *Nature Reviews Materials* **6**, 201 (2021).
- [10] F. Wu, T. Lovorn, E. Tutuc, and A. H. MacDonald, Hubbard model physics in transition metal dichalcogenide moiré bands, *Phys. Rev. Lett.* **121**, 026402 (2018).
- [11] H. Pan, F. Wu, and S. Das Sarma, Band topology, hubbard model, heisenberg model, and dzyaloshinskii-moriya interaction in twisted bilayer wse_2 , *Phys. Rev. Research* **2**, 033087 (2020).
- [12] H. Pan, F. Wu, and S. Das Sarma, Quantum phase diagram of a moiré-hubbard model, *Phys. Rev. B* **102**, 201104 (2020).
- [13] H. Pan and S. Das Sarma, Interaction range and temperature dependence of symmetry breaking in strongly correlated two-dimensional moiré transition metal dichalcogenide bilayers, *Phys. Rev. B* **105**, 041109 (2022).
- [14] N. Morales-Durán, N. C. Hu, P. Potasz, and A. H. MacDonald, Nonlocal interactions in moiré hubbard systems, *Phys. Rev. Lett.* **128**, 217202 (2022).
- [15] Y. Tang, L. Li, T. Li, Y. Xu, S. Liu, K. Barmak, K. Watanabe, T. Taniguchi, A. H. MacDonald, J. Shan, and K. F. Mak, Simulation of hubbard model physics in wse_2/ws_2 moiré superlattices, *Nature* **579**, 353 (2020).
- [16] Y. Shimazaki, I. Schwartz, K. Watanabe, T. Taniguchi, M. Kroner, and A. Imamoğlu, Strongly correlated electrons and hybrid excitons in a moiré heterostructure, *Nature* **580**, 472 (2020).
- [17] L. Wang, E.-M. Shih, A. Ghiotto, L. Xian, D. A. Rhodes, C. Tan, M. Claassen, D. M. Kennes, Y. Bai, B. Kim, K. Watanabe, T. Taniguchi, X. Zhu, J. Hone, A. Rubio, A. N. Pasupathy, and C. R. Dean, Correlated electronic phases in twisted bilayer transition metal dichalcogenides, *Nature Materials* **19**, 861 (2020).
- [18] E. C. Regan, D. Wang, C. Jin, M. I. Bakti Utama, B. Gao, X. Wei, S. Zhao, W. Zhao, Z. Zhang, K. Yumigeta, M. Blei, J. D. Carlström, K. Watanabe, T. Taniguchi, S. Tongay, M. Crommie, A. Zettl, and F. Wang, Mott and generalized wigner crystal states in wse_2/ws_2 moiré superlattices, *Nature* **579**, 359 (2020).
- [19] Y. Xu, S. Liu, D. A. Rhodes, K. Watanabe, T. Taniguchi, J. Hone, V. Elser, K. F. Mak, and J. Shan, Correlated insulating states at fractional fillings of moiré superlattices, *Nature* **587**, 214 (2020).
- [20] X. Huang, T. Wang, S. Miao, C. Wang, Z. Li, Z. Lian, T. Taniguchi, K. Watanabe, S. Okamoto, D. Xiao, S.-F. Shi, and Y.-T. Cui, Correlated insulating states at fractional fillings of the ws_2/wse_2 moiré lattice, *Nature Physics* **17**, 715 (2021).
- [21] C. Jin, Z. Tao, T. Li, Y. Xu, Y. Tang, J. Zhu, S. Liu, K. Watanabe, T. Taniguchi, J. C. Hone, L. Fu, J. Shan, and K. F. Mak, Stripe phases in wse_2/ws_2 moiré superlattices, *Nature Materials* **20**, 940 (2021).
- [22] H. Li, S. Li, E. C. Regan, D. Wang, W. Zhao, S. Kahn, K. Yumigeta, M. Blei, T. Taniguchi, K. Watanabe, S. Tongay, A. Zettl, M. F. Crommie, and F. Wang, Imaging two-dimensional generalized wigner crystals, *Nature* **597**, 650 (2021).
- [23] T. Smoleński, P. E. Dolgirev, C. Kuhlenkamp, A. Popert, Y. Shimazaki, P. Back, X. Lu, M. Kroner, K. Watanabe, T. Taniguchi, I. Esterlis, E. Demler, and A. Imamoğlu, Signatures of wigner crystal of electrons in a monolayer semiconductor, *Nature* **595**, 53 (2021).
- [24] T. Li, S. Jiang, B. Shen, Y. Zhang, L. Li, Z. Tao, T. Devakul, K. Watanabe, T. Taniguchi, L. Fu, J. Shan, and K. F. Mak, Quantum anomalous hall effect from intertwined moiré bands, *Nature* **600**, 641 (2021).
- [25] J. Cai, E. Anderson, C. Wang, X. Zhang, X. Liu, W. Holtzmann, Y. Zhang, F. Fan, T. Taniguchi, K. Watanabe, Y. Ran, T. Cao, L. Fu, D. Xiao, W. Yao, and X. Xu, Signatures of fractional quantum anomalous hall states in twisted mote_2 , *Nature* **622**, 63 (2023).
- [26] M. Sidler, P. Back, O. Cotlet, A. Srivastava, T. Fink, M. Kroner, E. Demler, and A. Imamoğlu, Fermi polaron-polaritons in charge-tunable atomically thin semiconductors, *Nature Physics* **13**, 255 (2017).
- [27] L. B. Tan, O. K. Diessel, A. Popert, R. Schmidt, A. Imamoğlu, and M. Kroner, Bose polaron interactions in a cavity-coupled monolayer semiconductor, *Phys. Rev. X* **13**, 031036 (2023).
- [28] F. P. Laussy, A. V. Kavokin, and I. A. Shelykh, Exciton-polariton mediated superconductivity, *Phys. Rev. Lett.* **104**, 106402 (2010).
- [29] O. Cotlet, S. Zeytinoglu, M. Sigrist, E. Demler, and A. m. c. Imamoğlu, Superconductivity and other collective phenomena in a hybrid bose-fermi mixture formed by a polariton condensate and an electron system in two dimensions, *Phys. Rev. B* **93**, 054510 (2016).
- [30] A. Julku, J. J. Kinnunen, A. Camacho-Guardian, and G. M. Bruun, Light-induced topological superconductivity in transition metal dichalcogenide monolayers, *Phys.*

- Rev. B **106**, 134510 (2022).
- [31] J. von Milczewski, X. Chen, A. Imamoglu, and R. Schmidt, Superconductivity induced by strong electron-exciton coupling in doped atomically thin semiconductor heterostructures (2023), [arXiv:2310.10726](https://arxiv.org/abs/2310.10726) [[cond-mat.mes-hall](https://arxiv.org/abs/2310.10726)].
- [32] C. Zerba, C. Kuhlenkamp, A. Imamoglu, and M. Knap, Realizing topological superconductivity in tunable bose-fermi mixtures with transition metal dichalcogenide heterostructures (2023), [arXiv:2310.10720](https://arxiv.org/abs/2310.10720) [[cond-mat.mes-hall](https://arxiv.org/abs/2310.10720)].
- [33] K. Hejazi, Z.-X. Luo, and L. Balents, Noncollinear phases in moiré magnets, *Proceedings of the National Academy of Sciences* **117**, 10721 (2020), <https://www.pnas.org/doi/pdf/10.1073/pnas.2000347117>.
- [34] N. Morales-Durán, P. Potasz, and A. H. MacDonald, Magnetism and quantum melting in moiré-material wigner crystals, *Phys. Rev. B* **107**, 235131 (2023).
- [35] D. Kiese, Y. He, C. Hickey, A. Rubio, and D. M. Kennes, TMDs as a platform for spin liquid physics: A strong coupling study of twisted bilayer WSe₂, *APL Materials* **10**, 10.1063/5.0077901 (2022), 031113, https://pubs.aip.org/aip/apm/article-pdf/doi/10.1063/5.0077901/16490454/031113_1.online.pdf.
- [36] J. Zang, J. Wang, J. Cano, and A. J. Millis, Hartree-Fock study of the moiré hubbard model for twisted bilayer transition metal dichalcogenides, *Phys. Rev. B* **104**, 075150 (2021).
- [37] J. Zang, J. Wang, J. Cano, A. Georges, and A. J. Millis, Dynamical mean-field theory of moiré bilayer transition metal dichalcogenides: Phase diagram, resistivity, and quantum criticality, *Phys. Rev. X* **12**, 021064 (2022).
- [38] T. Li, S. Jiang, L. Li, Y. Zhang, K. Kang, J. Zhu, K. Watanabe, T. Taniguchi, D. Chowdhury, L. Fu, J. Shan, and K. F. Mak, Continuous mott transition in semiconductor moiré superlattices, *Nature* **597**, 350 (2021).
- [39] L. Ciorciaro, T. Smolenski, I. Morera, N. Kiper, S. Hiestand, M. Kroner, Y. Zhang, K. Watanabe, T. Taniguchi, E. Demler, and A. Imamoglu, Kinetic magnetism in triangular moiré materials (2023), [arXiv:2305.02150](https://arxiv.org/abs/2305.02150) [[cond-mat.str-el](https://arxiv.org/abs/2305.02150)].
- [40] A. Ghiotto, E.-M. Shih, G. S. S. G. Pereira, D. A. Rhodes, B. Kim, J. Zang, A. J. Millis, K. Watanabe, T. Taniguchi, J. C. Hone, L. Wang, C. R. Dean, and A. N. Pasupathy, Quantum criticality in twisted transition metal dichalcogenides, *Nature* **597**, 345 (2021).
- [41] M. Drescher, L. Vanderstraeten, R. Moessner, and F. Pollmann, Dynamical signatures of symmetry broken and liquid phases in an $s = 1/2$ heisenberg antiferromagnet on the triangular lattice (2022), [arXiv:2209.03344](https://arxiv.org/abs/2209.03344) [[cond-mat.str-el](https://arxiv.org/abs/2209.03344)].
- [42] N. E. Sherman, M. Dupont, and J. E. Moore, Spectral function of the $J_1 - J_2$ heisenberg model on the triangular lattice, *Phys. Rev. B* **107**, 165146 (2023).
- [43] C. Kuhlenkamp, W. Kadow, A. Imamoglu, and M. Knap, Tunable topological order of pseudo spins in semiconductor heterostructures (2022), [arXiv:2209.05506](https://arxiv.org/abs/2209.05506) [[cond-mat.str-el](https://arxiv.org/abs/2209.05506)].
- [44] S. Calder, A. I. Kolesnikov, and A. F. May, Magnetic excitations in the quasi-two-dimensional ferromagnet $\text{Fe}_{3-x}\text{GeTe}_2$ measured with inelastic neutron scattering, *Phys. Rev. B* **99**, 094423 (2019).
- [45] M. Papaj and C. Lewandowski, Probing correlated states with plasmons, *Science Advances* **9**, eadg3262 (2023), <https://www.science.org/doi/pdf/10.1126/sciadv.adg3262>.
- [46] D. A. Ruiz-Tijerina and V. I. Fal'ko, Interlayer hybridization and moiré superlattice minibands for electrons and excitons in heterobilayers of transition-metal dichalcogenides, *Phys. Rev. B* **99**, 125424 (2019).
- [47] E. M. Alexeev, D. A. Ruiz-Tijerina, M. Danovich, M. J. Hamer, D. J. Terry, P. K. Nayak, S. Ahn, S. Pak, J. Lee, J. I. Sohn, M. R. Molas, M. Koperski, K. Watanabe, T. Taniguchi, K. S. Novoselov, R. V. Gorbachev, H. S. Shin, V. I. Fal'ko, and A. I. Tartakovskii, Resonantly hybridized excitons in moiré superlattices in van der waals heterostructures, *Nature* **567**, 81 (2019).
- [48] A. Julku, Nonlocal interactions and supersolidity of moiré excitons, *Phys. Rev. B* **106**, 035406 (2022).
- [49] I. Schwartz, Y. Shimazaki, C. Kuhlenkamp, K. Watanabe, T. Taniguchi, M. Kroner, and A. Imamoglu, Electrically tunable feshbach resonances in twisted bilayer semiconductors, *Science* **374**, 336 (2021).
- [50] C. Kuhlenkamp, M. Knap, M. Wagner, R. Schmidt, and A. m. c. Imamoglu, Tunable feshbach resonances and their spectral signatures in bilayer semiconductors, *Phys. Rev. Lett.* **129**, 037401 (2022).
- [51] D. K. Efimkin, E. K. Laird, J. Levinsen, M. M. Parish, and A. H. MacDonald, Electron-exciton interactions in the exciton-polaron problem, *Phys. Rev. B* **103**, 075417 (2021).
- [52] M. Wouters, Resonant polariton-polariton scattering in semiconductor microcavities, *Phys. Rev. B* **76**, 045319 (2007).
- [53] I. Carusotto, T. Volz, and A. Imamoglu, Feshbach blockade: Single-photon nonlinear optics using resonantly enhanced cavity polariton scattering from biexciton states, *EPL (Europhysics Letters)* **90**, 37001 (2010).
- [54] M. A. Bastarrachea-Magnani, A. Camacho-Guardian, M. Wouters, and G. M. Bruun, Strong interactions and biexcitons in a polariton mixture, *Phys. Rev. B* **100**, 195301 (2019).
- [55] L. B. Tan, O. Cotlet, A. Bergschneider, R. Schmidt, P. Back, Y. Shimazaki, M. Kroner, and A. m. c. Imamoglu, Interacting polaron-polaritons, *Phys. Rev. X* **10**, 021011 (2020).
- [56] Z. Liu and E. Manousakis, Dynamical properties of a hole in a heisenberg antiferromagnet, *Phys. Rev. B* **45**, 2425 (1992).
- [57] A. E. Trumper, C. J. Gazza, and L. O. Manuel, Quasiparticle vanishing driven by geometrical frustration, *Phys. Rev. B* **69**, 184407 (2004).
- [58] I. J. Hamad, A. E. Trumper, A. E. Feiguin, and L. O. Manuel, Spin polaron in the $J_1 - J_2$ heisenberg model, *Phys. Rev. B* **77**, 014410 (2008).
- [59] E. Manousakis, String excitations of a hole in a quantum antiferromagnet and photoelectron spectroscopy, *Phys. Rev. B* **75**, 035106 (2007).
- [60] Y. Shimazaki, C. Kuhlenkamp, I. Schwartz, T. Smoleński, K. Watanabe, T. Taniguchi, M. Kroner, R. Schmidt, M. Knap, and A. m. c. Imamoglu, Optical signatures of periodic charge distribution in a mott-like correlated insulator state, *Phys. Rev. X* **11**, 021027 (2021).
- [61] S. Miao, T. Wang, X. Huang, D. Chen, Z. Lian, C. Wang, M. Blei, T. Taniguchi, K. Watanabe, S. Tongay, Z. Wang, D. Xiao, Y.-T. Cui, and S.-F. Shi, Strong interaction between interlayer excitons and correlated electrons in

- wse₂/ws₂ moiré superlattice, *Nature Communications* **12**, 3608 (2021).
- [62] A. G. Salvador, C. Kuhlenkamp, L. Ciorciaro, M. Knap, and A. m. c. İmamoglu, Optical signatures of periodic magnetization: The moiré zeeman effect, *Phys. Rev. Lett.* **128**, 237401 (2022).
- [63] Y. Iqbal, W.-J. Hu, R. Thomale, D. Poilblanc, and F. Becca, Spin liquid nature in the heisenberg $J_1 - J_2$ triangular antiferromagnet, *Phys. Rev. B* **93**, 144411 (2016).
- [64] J. van de Kraats, K. K. Nielsen, and G. M. Bruun, Holes and magnetic polarons in a triangular lattice antiferromagnet, *Phys. Rev. B* **106**, 235143 (2022).
- [65] A. L. Chernyshev and M. E. Zhitomirsky, Spin waves in a triangular lattice antiferromagnet: Decays, spectrum renormalization, and singularities, *Phys. Rev. B* **79**, 144416 (2009).
- [66] F. Ferrari and F. Becca, Dynamical structure factor of the $J_1 - J_2$ heisenberg model on the triangular lattice: Magnons, spinons, and gauge fields, *Phys. Rev. X* **9**, 031026 (2019).
- [67] B. Keimer, S. A. Kivelson, M. R. Norman, S. Uchida, and J. Zaanen, From quantum matter to high-temperature superconductivity in copper oxides, *Nature* **518**, 179 (2015).
- [68] H.-H. Wen and S. Li, Materials and novel superconductivity in iron pnictide superconductors, *Annual Review of Condensed Matter Physics* **2**, 121 (2011), <https://doi.org/10.1146/annurev-conmatphys-062910-140518>.
- [69] C. L. Kane, P. A. Lee, and N. Read, Motion of a single hole in a quantum antiferromagnet, *Phys. Rev. B* **39**, 6880 (1989).
- [70] G. Martinez and P. Horsch, Spin polarons in the t-j model, *Phys. Rev. B* **44**, 317 (1991).
- [71] Z. Liu and E. Manousakis, Spectral function of a hole in the t-j model, *Phys. Rev. B* **44**, 2414 (1991).
- [72] N. G. Diamantis and E. Manousakis, Dynamics of string-like states of a hole in a quantum antiferromagnet: a diagrammatic monte carlo simulation, *New Journal of Physics* **23**, 123005 (2021).
- [73] K. K. Nielsen, M. A. Bastarrachea-Magnani, T. Pohl, and G. M. Bruun, Spatial structure of magnetic polarons in strongly interacting antiferromagnets, *Phys. Rev. B* **104**, 155136 (2021).
- [74] K. K. Nielsen, T. Pohl, and G. M. Bruun, Nonequilibrium hole dynamics in antiferromagnets: Damped strings and polarons, *Phys. Rev. Lett.* **129**, 246601 (2022).
- [75] T.-S. Huang, Y.-Z. Chou, C. L. Baldwin, F. Wu, and M. Hafezi, Mott-moiré excitons, *Phys. Rev. B* **107**, 195151 (2023).
- [76] J. Shi and A. H. MacDonald, Magnetic states of graphene proximitized kitaev materials, *Physical Review B* **108**, 10.1103/physrevb.108.064401 (2023).
- [77] K. Marinov, A. Avsar, K. Watanabe, T. Taniguchi, and A. Kis, Resolving the spin splitting in the conduction band of monolayer mos₂, *Nature Communications* **8**, 1938 (2017).
- [78] J. Hong, R. Senga, T. Pichler, and K. Suenaga, Probing exciton dispersions of freestanding monolayer wse₂ by momentum-resolved electron energy-loss spectroscopy, *Phys. Rev. Lett.* **124**, 087401 (2020).
- [79] U. Zondiner, A. Rozen, D. Rodan-Legrain, Y. Cao, R. Queiroz, T. Taniguchi, K. Watanabe, Y. Oreg, F. von Oppen, A. Stern, E. Berg, P. Jarillo-Herrero, and S. Ilani, Cascade of phase transitions and dirac revivals in magic-angle graphene, *Nature* **582**, 203 (2020).
- [80] F. Wu, T. Lovorn, and A. H. MacDonald, Topological exciton bands in moiré heterojunctions, *Phys. Rev. Lett.* **118**, 147401 (2017).
- [81] H. Yu, G.-B. Liu, J. Tang, X. Xu, and W. Yao, Moiré excitons: From programmable quantum emitter arrays to spin-orbit-coupled artificial lattices, *Science Advances* **3**, e1701696 (2017), <https://www.science.org/doi/pdf/10.1126/sciadv.1701696>.
- [82] L. Zhang, F. Wu, S. Hou, Z. Zhang, Y.-H. Chou, K. Watanabe, T. Taniguchi, S. R. Forrest, and H. Deng, Van der waals heterostructure polaritons with moiré-induced nonlinearity, *Nature* **591**, 61 (2021).
- [83] I. Carusotto and C. Ciuti, Probing microcavity polariton superfluidity through resonant rayleigh scattering, *Phys. Rev. Lett.* **93**, 166401 (2004).
- [84] P. Massignan, M. Zaccanti, and G. M. Bruun, Polarons, dressed molecules and itinerant ferromagnetism in ultracold fermi gases, *Reports on Progress in Physics* **77**, 034401 (2014).
- [85] H. Terrones, F. López-Urías, and M. Terrones, Novel hetero-layered materials with tunable direct band gaps by sandwiching different metal disulfides and diselenides, *Scientific Reports* **3**, 1549 (2013).
- [86] T. Mueller and E. Malic, Exciton physics and device application of two-dimensional transition metal dichalcogenide semiconductors, *npj 2D Materials and Applications* **2**, 29 (2018).
- [87] Y. Wang, Z. Wang, W. Yao, G.-B. Liu, and H. Yu, Interlayer coupling in commensurate and incommensurate bilayer structures of transition-metal dichalcogenides, *Phys. Rev. B* **95**, 115429 (2017).
- [88] A. V. Chubukov and S. A. Kivelson, Superconductivity in engineered two-dimensional electron gases, *Phys. Rev. B* **96**, 174514 (2017).
- [89] M. Danovich, D. A. Ruiz-Tijerina, R. J. Hunt, M. Szyniszewski, N. D. Drummond, and V. I. Fal'ko, Localized interlayer complexes in heterobilayer transition metal dichalcogenides, *Phys. Rev. B* **97**, 195452 (2018).
- [90] A. H. MacDonald, S. M. Girvin, and D. Yoshioka, $\frac{t}{U}$ expansion for the hubbard model, *Phys. Rev. B* **37**, 9753 (1988).